



**HAL**  
open science

## A comprehensive experimental and kinetic modeling study of di-isobutylene isomers: Part 2

Nitin Lokachari, Goutham Kukkadapu, Brian D Etz, Gina M Fioroni, Seonah Kim, Mathias Steglich, Andras Bodi, Patrick Hemberger, Sergey S Matveev, Anna Thomas, et al.

► **To cite this version:**

Nitin Lokachari, Goutham Kukkadapu, Brian D Etz, Gina M Fioroni, Seonah Kim, et al.. A comprehensive experimental and kinetic modeling study of di-isobutylene isomers: Part 2. *Combustion and Flame*, 2022, 251, pp.112547. 10.1016/j.combustflame.2022.112547 . hal-04523993v2

**HAL Id: hal-04523993**

**<https://hal.science/hal-04523993v2>**

Submitted on 27 Mar 2024

**HAL** is a multi-disciplinary open access archive for the deposit and dissemination of scientific research documents, whether they are published or not. The documents may come from teaching and research institutions in France or abroad, or from public or private research centers.

L'archive ouverte pluridisciplinaire **HAL**, est destinée au dépôt et à la diffusion de documents scientifiques de niveau recherche, publiés ou non, émanant des établissements d'enseignement et de recherche français ou étrangers, des laboratoires publics ou privés.



Contents lists available at ScienceDirect

# Combustion and Flame

journal homepage: [www.elsevier.com/locate/combustflame](http://www.elsevier.com/locate/combustflame)

## A comprehensive experimental and kinetic modeling study of di-isobutylene isomers: Part 2



Nitin Lokachari<sup>a</sup>, Goutham Kukkadapu<sup>b</sup>, Brian D. Etz<sup>c</sup>, Gina M. Fioroni<sup>c</sup>, Seonah Kim<sup>c,d</sup>, Mathias Steglich<sup>e</sup>, Andras Bodi<sup>e</sup>, Patrick Hemberger<sup>e</sup>, Sergey S. Matveev<sup>f</sup>, Anna Thomas<sup>c</sup>, Hwasup Song<sup>g,i</sup>, Guillaume Vanhove<sup>g</sup>, Kuiwen Zhang<sup>b</sup>, Guillaume Dayma<sup>h</sup>, Maxence Lailliau<sup>h</sup>, Zeynep Serinyel<sup>h</sup>, Alexander A. Konnov<sup>j,\*</sup>, Philippe Dagaut<sup>h</sup>, William J. Pitz<sup>b</sup>, Henry J. Curran<sup>a</sup>

<sup>a</sup> Combustion Chemistry Centre, School of Biological and Chemical Sciences, Ryan Institute, MaREI, University of Galway, Galway, Ireland

<sup>b</sup> Lawrence Livermore National Laboratory, Livermore, CA 94551, United States

<sup>c</sup> National Renewable Energy Laboratory, Golden, CO 80401, United States

<sup>d</sup> Department of Chemistry, Colorado State University, Fort Collins, CO 80523, United States

<sup>e</sup> Laboratory for Femtochemistry and Synchrotron Radiation, Paul Scherrer Institute, Villigen 5232, Switzerland

<sup>f</sup> Scientific and Educational Centre of Fluid Dynamics Research, Samara National Research University, Samara, Russia

<sup>g</sup> University of Lille, CNRS, UMR 8522 - PC2A - Physicochimie des Processus de Combustion et de l'Atmosphère, Lille F-59000, France

<sup>h</sup> CNRS-INSIS, Institut de Combustion, Aérodynamique, Réactivité et Environnement, Orléans, France

<sup>i</sup> Department of Mechanical Engineering, Kumoh National Institute of Technology, 61 Daehak-ro, Gumi, Gyeongsangbuk-do 39177, South Korea

<sup>j</sup> Division of Combustion Physics, Lund University, Lund, Sweden

### ARTICLE INFO

#### Article history:

Received 23 May 2022

Revised 22 November 2022

Accepted 25 November 2022

Available online 13 December 2022

#### Keywords:

Di-isobutylene

Pyrolysis, ignition delay

Burning velocity

Kinetic modeling

### ABSTRACT

A wide variety of high temperature experimental data obtained in this study complement the data on the oxidation of the two di-isobutylene isomers presented in Part I and offers a basis for an extensive validation of the kinetic model developed in this study. Due to the increasing importance of unimolecular decomposition reactions in high-temperature combustion, we have investigated the di-isobutylene isomers in high dilution utilizing a pyrolysis microflow reactor and detected radical intermediates and stable products using vacuum ultraviolet (VUV) synchrotron radiation and photoelectron photoion coincidence (PEPICO) spectroscopy. Additional speciation data at oxidative conditions were also recorded utilizing a plug flow reactor at atmospheric pressure in the temperature range 725–1150 K at equivalence ratios of 1.0 and 3.0 and at residence times of 0.35 s and 0.22 s, respectively. Combustion products were analyzed using gas chromatography (GC) and mass spectrometry (MS). Ignition delay time measurements for di-isobutylene were performed at pressures of 15 and 30 bar at equivalence ratios of 0.5, 1.0, and 2.0 diluted in 'air' in the temperature range 900–1400 K using a high-pressure shock-tube facility. New measurements of the laminar burning velocities of di-isobutylene/air flames are also presented. The experiments were performed using the heat flux method at atmospheric pressure and initial temperatures of 298–358 K. Moreover, data consistency was assessed with the help of analysis of the temperature and pressure dependencies of laminar burning velocity measurements, which was interpreted using an empirical power-law expression. Electronic structure calculations were performed to compute the energy barriers to the formation of many of the product species formed. The predictions of the present mechanism were found to be in adequate agreement with the wide variety of experimental measurements performed.

© 2022 The Author(s). Published by Elsevier Inc. on behalf of The Combustion Institute.

This is an open access article under the CC BY license (<http://creativecommons.org/licenses/by/4.0/>)

### 1. Introduction

As highlighted in Part I [1] of this study, di-isobutylene has been identified as one of six blendstocks made from biomass that give the highest efficiency gains for downsized, boosted, spark-ignition (SI) engines and has the fewest barriers towards imple-

\* Corresponding author.

E-mail address: [alexander.konnov@forbrf.lth.se](mailto:alexander.konnov@forbrf.lth.se) (A.A. Konnov).

**Table 1**  
Laminar burning velocity measurements of di-isobutylene/air flames.

Fuel	Pressure (atm)	Temperature (K)	$\varphi$	Method	Source
DIB	1	377–455	~1	Bunsen burner	[12]
DIB-1	1, 3	400, 450	0.6–1.5	Spherical flame	[13]
DIB-1	1, 3, 5	298, 373, 453	0.7–1.6	Spherical flame	[15]
DIB-2	1	298, 373, 453	0.8–1.6	Spherical flame	[17]
DIB-1	1	428	0.9–1.5	Spherical flame	[21]
DIB	1	298, 318, 338, 358	0.7–1.4	Heat flux burner	p.w.

mentation in the ground transportation market [2]. The name di-isobutylene is usually applied to a mixture of two isomers: 2,4,4-trimethyl-1-pentene and 2,4,4-trimethyl-2-pentene, abbreviated here as DIB-1 and DIB-2, respectively. In the market, di-isobutylene is often available as a mixture of DIB-1 and DIB-2 in a 3:1 ratio and will be abbreviated as DIB.

Part I of this study exclusively focuses on the low-to-intermediate temperature kinetics of DIB; ignition delay times (IDTs) and speciation measurements were obtained in a rapid compression machine and in a jet-stirred reactor, respectively, during DIB oxidation and were validated with a new detailed kinetic mechanism to describe its oxidation. Here we present an investigation of the high-temperature model development and validation on the relevant experimental targets, such as IDTs and laminar burning velocities (LBVs) of DIB across a wide range of conditions. In [2], more than 400 blendstocks (compounds and fuel mixtures) were considered and were down selected to forty blendstocks with desirable fuel properties for advanced SI engines [3]. Thereafter, the list of compounds was further refined based on a merit function used to identify blendstocks that gave the highest efficiency gain in a downsized, boosted SI engine. The most important input to the merit function was the research octane number (RON) and octane sensitivity of the blendstocks [4]. Finally, the list was narrowed down based on techno-economic and life-cycle analyses, including a criterion that the blendstock would reduce greenhouse gas emission by at least 60% compared to petroleum-based fuels. This yielded six blendstocks, including DIB, with the fewest barriers to market.

To the best of our knowledge, no study exists investigating the unimolecular decomposition of the two isomers under anaerobic conditions. This has motivated us to study unimolecular decomposition of DIB in a pyrolysis micro-reactor, which is more relevant at high temperature ( $\geq 1100$  K) combustion conditions. The first dedicated study of DIB-1 and DIB-2 oxidation in a shock tube allowed for the development and first validation of a detailed kinetic model by Metcalfe et al. [5]. Mixtures of primary reference fuels (PRFs) with DIB have also been studied in a shock tube [6]. Subsequent studies in shock tubes were aimed at improving the Metcalfe et al. [5] model by Hu et al. [7] or construction of a new model (also based on [5]) by Li et al. [8]. Later Yin et al. [9] showed that the low-temperature chemistry is dominated by hydrogen abstraction reactions.

Recent work by Terracciano et al. [10] examined both DIB-1 and DIB-2 at stoichiometric conditions and at atmospheric pressure in a jet-stirred reactor and identified intermediates using tunable vacuum ultraviolet (VUV) and time-of-flight mass spectrometry. They found that the ignition characteristics were greatly dependent on  $C_4$  and  $C_7$  fragment production and decomposition for both isomers and that the tert-butyl radical was a dominant intermediate species. Additionally, the DIB-1 isomer produced larger quantities of  $C_4$  over  $C_7$  compounds, while the opposite result was found for the DIB-2 isomer, with it favoring  $C_7$  over  $C_4$  compounds.

The adiabatic laminar burning velocity,  $S_L$ , plays an important role in rate of fuel oxidation in SI engines, therefore its determination for different hydrocarbons has a long history [11]. The first  $S_L$

measurements for DIB/air near-stoichiometric mixtures were performed by Albright et al. [12] at atmospheric pressure at several initial temperatures in the temperature range of 377–455 K using the flame cone method. The authors noted that the variation of burning velocity with temperature is different for various hydrocarbons, while the rate of change for DIB is lowest compared to *n*-hexane, *n*-heptane, *iso*-octane, and toluene.

Revitalized interest in DIB as a fuel supplement inspired several recent flame studies summarized in Table 1. Zheng et al. [13] measured burning velocities of DIB-1/air flames in a constant volume combustion bomb at initial mixture temperatures of 400 and 450 K, at 1 and 3 atm, comparing linear and non-linear stretch correction approaches. These measurements were compared to the predictions of the kinetic model developed by Andrae and Kovács [14], and the mechanism developed by the authors [13]. The model of Zheng et al. [13] combines the di-isobutylene sub-mechanism by Metcalfe et al. [5] with a reduced core  $C_0$ – $C_4$  model based on the USC-II mechanism.

Hu et al. [15] determined burning velocities of DIB-1/air flames in a broad range of temperatures from 298 to 453 K and at 1, 3, and 5 atm in spherical flames applying the non-linear stretch correction. The authors found that the model from Metcalfe et al. [5] notably over-predicts their  $S_L$  measurements and suggested several modifications to improve its performance. First, the core  $C_0$ – $C_4$  model was replaced by AramcoMech2.0 [16], and second, high-level ab initio calculations were used to update several rate constants of important DIB-1 reactions. Moreover, the temperature and pressure dependencies of the burning velocity were interpreted using the following empirical equation [11]:

$$S_L = S_{L0} (T/T_0)^\alpha (p/p_0)^\beta \quad (1)$$

which relates the burning velocity,  $S_L$ , at initial temperature  $T$  and pressure  $p$  to that at the reference temperature  $T_0$  and pressure  $p_0$ . The power exponents  $\alpha$  and  $\beta$  were approximated by polynomial functions of the equivalence ratio  $\varphi$  [15].

A subsequent study from the same group [17] aimed to determine the burning velocity of DIB-2 at 1 atm and the same initial temperatures of 298, 373, and 453 K allowing for direct comparison with DIB-1 [15]  $S_L$  measurements. It was found that DIB-2 burns faster than DIB-1, with the difference increasing from 1 to 2 cm s<sup>-1</sup> for lean flames, to 5–7 cm s<sup>-1</sup> in rich flames at both room and elevated temperatures. The model presented by Hu et al. [15] was found to be in better agreement with the burning velocities of DIB-2 compared to the Metcalfe et al. [5] model.

Further development of the kinetic model for DIB-1 oxidation was presented by Yin et al. [18]. The model improvement was achieved by modification of the rate constants of the primary radicals' isomerization, decomposition, reactions with  $O_2$  as well as H-atom abstraction reactions. These rate constants were derived using high-level quantum chemical calculations [9,18–20], and improved agreement with available experimental data for DIB-1 IDTs and  $S_L$ s of rich flames compared to the Metcalfe et al. [5] model was demonstrated. Yin et al. [18] concluded that their modified model exhibits "reasonable agreement" with the shock tube data and laminar flame speeds, which calls for further analysis of DIB

oxidation at high temperatures based on additional experiments which have been performed here.

Most recently the burning velocities of DIB-1 were determined in spherical flames at 1 atm and at an initial temperature of 428 K [21]. Laich et al. implemented a multi-zone model to derive LBVs from pressure traces and thus ignored stretch correction. These measurements [21] were compared with the results of Zheng et al. at 1 atm and appeared to be slightly higher (for fuel-lean mixtures) or lower (for fuel-rich mixtures) compared to the LBVs measured by Zheng et al. at 450 K [13].

A common approach to validate detailed kinetic mechanisms is to compare model predictions with the experimental data in coordinates of  $S_L$  vs.  $\phi$ , for a given initial  $p$  and  $T$ . However, this assessment is often possible for one dataset only, since the measurements are seldom performed at the same conditions, as shown in Table 1. To this end, analysis of the temperature and pressure dependencies of the burning velocity interpreted in Eq. (1) can help compare experimental results obtained at different conditions [11]. Therefore, the objective of the present work is to determine LBVs of DIB/air flames at atmospheric pressure and different temperatures and analyze data consistency of the new results and experiments available in the literature.

Additionally, in this study, unique speciation data were obtained in a microflow tube reactor at pyrolytic conditions as well as in a flow reactor at stoichiometric and fuel-rich conditions to further improve the model. Moreover, new measurements of IDTs in a high-pressure shock tube (HPST) extend the range of temperatures covered in rapid compression machines as presented in Part I [1].

The following paper is structured by first providing an overview of the experimental methodologies adopted in this study in Section 2, followed by a brief description of our DFT analyses and high-temperature kinetic modeling of DIB in Section 3. A discussion of the important findings from this study and model validation using the new data follows in Section 4 and a summary along with recommendations for future work are presented in Section 5.

## 2. Experimental methods

### 2.1. Microflow tube reactor (PSI)

The pyrolysis experiments of the two di-isobutylene isomers were performed at the Vacuum Ultraviolet [22,23] beamline of the Swiss Light Source, Paul Scherrer Institute (PSI), Switzerland. The di-isobutylene samples were diluted (0.05%) in Ar to suppress bimolecular chemistry and expanded through a 100  $\mu\text{m}$  pinhole into a resistively heated silicon carbide microreactor (40 mm length, 2 mm oD, 1 mm iD). The temperature of this Chen-type reactor was varied from room temperature to 1600 K [24]. The effective pressure and residence time in the microreactor were outlined by Guan et al. [25] and Grimm et al. [26] and are in the range of 9–20 mbar and 25–50  $\mu\text{s}$ , respectively. Due to the small inner diameter (1 mm) a direct measurement of the gas temperature is not possible without disturbing the flow conditions. We thus obtained only the wall temperature, which may overestimate the gas temperature by up to 200 K according to Guan et al. [25]. The gas mixture leaving the reactor expands into high vacuum ( $10^{-5}$  mbar), where a molecular beam is formed, which preserves the reaction mixture, including reactive free radicals, thus providing a snapshot of the unimolecular chemistry at the specific temperature. The reaction mixture in the expanding molecular beam is skimmed (2 mm skimmer) and travels into the ionization volume of the Photoelectron Photoion Coincidence (PEPICO) end-station, where it is intersected with the vacuum ultraviolet synchrotron (VUV) radiation [27,28]. A bending magnet produces the VUV synchrotron radiation, which is collimated onto a plane grating (150 l/mm), monochromatized, and focused onto the exit slit ( $E/\Delta E = 1500$ ).

Higher order radiation, also diffracted by the grating, is eliminated using a rare gas filter with an Ar/Ne/Kr mixture, or by a  $\text{MgF}_2$  window, as described in [23]. The PEPICO endstation was utilized to record photoionization mass spectra (PIMS) at different photon energies to observe reactive intermediates and products as function of the temperature. PIMS were recorded for typically 60–120 s, and the integrated  $m/z$  peaks were plotted as function of the temperature to obtain the species profiles. To measure photoion mass-selected threshold photoelectron (ms-TPE) spectra, we scanned the photon energies in 10–20 meV steps (averaged for 2–10 min per point) to obtain well-resolved vibrational transitions from the neutral into the ion. This structure provides isomer-specific information if compared to a reference or simulated spectra [28,29]. To do so, electrons with  $E_{\text{kin}} < 10$  meV were considered in the analysis, and the hot electron contribution to the center signal of the imaging detector, i.e., the electrons with significant kinetic energy in the non-off axis momentum component, was subtracted as outlined in the approach by Sztaray and Baer [30]. Due to the absence of reliable photoionization crosssection (PICS) for many of the intermediates and reaction products, the speciation data in Figs. 2 and 6 can only be seen as semi-quantitative.

### 2.2. Flow reactor (NREL)

The analysis of the di-isobutylene isomers was performed in a straight quartz tube flow reactor operated under atmospheric laboratory conditions (0.85 atmospheres) in Golden, Colorado. The flow reactor set up was previously described in detail [31–33]. In brief, the reactor consists of a straight quartz tube that is open on the backend and is heated inside a ceramic furnace. The temperature profile of the quartz tube was measured at one inch intervals throughout the length of the tube at each temperature examined and is incorporated into the simulations. Helium is utilized as the inert carrier gas and is introduced along with oxygen at the inlet of the quartz tube. The helium flow is adjusted to keep the residence time of 0.35 s for  $\phi = 1$  and 0.22 s for  $\phi = 3$  constant throughout the temperature sweep. Oxygen flow rates were 0.018 standard liters per minute (slm) for  $\phi = 1$ , and 0.0062 slm for  $\phi = 3$ . Helium flow rates ranged from 3.6 to 5.6 slm for  $\phi = 1$  and 5.9 to 8.0 slm for  $\phi = 3$ . Liquid fuel is introduced via a syringe pump operated at ambient laboratory conditions (20–22  $^{\circ}\text{C}$ ) at a flow rate of 10  $\mu\text{L}/\text{min}$  to maintain very dilute conditions (approximately 300 parts per million (ppm)) such that the stratification effect due to the parabolic velocity profile of the laminar tube reactor has a negligible effect on the sample mole fraction. Because the helium flow rate is adjusted throughout the experiment, the mole fractions of DIB varied between 190 ppm and 430 ppm. A DIB density value of 0.716 g/mL at 20  $^{\circ}\text{C}$  from the Sigma Aldrich certificate of analysis was utilized to calculate fuel concentrations at each temperature. A full list of experimental conditions and results is included in the Supplementary Material (Table S9). The effluent at the terminus of the reactor is sampled directly into an inert gas sampling line, heated to 95  $^{\circ}\text{C}$  to avoid any condensation of reaction products, into two separate gas chromatography (GC) systems used to measure and characterize the reaction species. The GC1 is equipped with two identical 60 m  $\times$  0.25  $\mu\text{m}$   $\times$  0.25  $\mu\text{m}$  DB-1 columns (Agilent Technologies) for simultaneous analysis of  $\geq \text{C}_4$  hydrocarbons quantitation utilizing a Flame Ionization Detector (FID) and positive identification by a mass spectrometer (MS). The GC2 utilizes a Dean switch with three columns; quantitation of the low molecular weight hydrocarbon gasses is performed using an FID. Carbon dioxide ( $\text{CO}_2$ ) and carbon monoxide (CO) are quantitated using two separate Thermal Conductivity Detectors (TCDs). The low molecular weight gasses are separated on a Restek Rt-Alumina BOND 30 m  $\times$  0.32  $\mu\text{m}$   $\times$  5  $\mu\text{m}$  column, while  $\text{CO}_2$  is quantitated on a Restek Rt-QPLOT 50 m  $\times$  0.32  $\mu\text{m}$   $\times$  5  $\mu\text{m}$  column, and CO is

quantitated on a Restek Rt Mol Sieve 30 m  $\times$  0.53  $\mu$ m  $\times$  50  $\mu$ m column. The GC1 is calibrated using *n*-heptane as a standard, and species were quantitated using the effective carbon number (ECN) method [34] based on *n*-heptane response. The GC2 is calibrated with standard gas mixtures of known concentration purchased from Matheson Gas. A  $\pm$  15% measurement uncertainty is assumed for GC1, which is due to the use of the ECN method, sample delivery/sampling system variations, as well as the relatively higher molecular weight species measured in this system. The GC2 quantifies lower molecular weight species which are easier to evaporate and have direct calibration standards and the associated uncertainty is assumed to be  $\pm$ 10%.

### 2.3. High-pressure shock-tube (NUIG)

The HPST at Galway has been described in detail previously [35] and is only discussed briefly here. It has a uniform cross-section area of 63.5 mm inner diameter consists of a 3 m long driver section to hold high pressure gas, 5.7 m long driven section that contains the test mixture and a 30 mm double diaphragm section with pre-scored aluminum discs of appropriate thickness, which separates the driver and driven sections and enables improved control over the shock wave generated.

By varying the Mach number of the shock wave, the final compressed conditions of the test gas are also varied. Part of helium driver gas is replaced with a heavier inert gas (nitrogen) to delay the arrival of the contact surface at the end-wall and to increase the measuring times ( $\geq$ 1.5 ms). Six PCB 113B24 piezoelectric pressure transducers are mounted on the side wall of the tube and one Kistler 603B sensor on the end-wall are used to extrapolate the shock velocity at the end-wall. The Kistler sensor is also used to record pressure profiles that are used to record/measure the IDTs. The measured shock velocity is used to calculate the compressed pressure and temperature using the 'reflected shock' routine in Gaseq [36]. The tolerance on the calculated pressure was limited to  $\pm$  0.5 bar of the target pressure and no pre-ignition pressure rise was observed during the experiments. The test fuel (DIB-1 98.5%) was supplied by Sigma Aldrich®. The other gasses used in this study, nitrogen (99.99%), oxygen (99.99%), argon (99.96%), and helium (99.97%), were purchased from BOC Ireland. The experimental measurements are given in Supplementary Material (Table S9).

### 2.4. Flat flames (Lund)

The heat flux method allows for the stabilization of a premixed, flat, non-stretched flame over the perforated burner plate and for determining the laminar burning velocity [37]. The method is based on the control of the temperature profile in the plate using thermocouples inserted in several perforation holes. When the flow rate of the unburned mixture is equal to the burning velocity of the adiabatic flame, the temperature profile is flat [37]. Thus, by varying the flow rate, the state of adiabatic flame stabilization can be accurately defined through interpolation. The heat flux required for the flame stabilization over the burner plate is realized by the difference in temperatures of the plenum chamber, which keeps the required initial temperature of the gas mixture and the heating jacket around the burner head, both controlled by water baths. Initial gas temperature in the present experiments was set in the 298–358 K range, while the temperature of the heating jacket was 368 K. At some conditions, often in rich flames of heavy hydrocarbons and/or when the temperature difference is relatively small, the flames become unstable. In this case, an extrapolation procedure is used, which still allows for the determination of the burning velocity, yet with somewhat higher experimental uncertainty. A review of the well-established heat flux method, its development, description of the experimental setup as well as of the

data processing algorithms was presented by Alekseev et al. [37]. DIB with a DIB-1/DIB-2 molar ratio of 3:1 and certified purity of 96.9% was delivered by Sigma-Aldrich, and the oxidizer was synthetic air (21% O<sub>2</sub> + 79% N<sub>2</sub> 1% relative uncertainty) delivered by Linde. The equivalence ratio,  $\phi$ , of the mixtures with air was varied from 0.7 to 1.4. All experimental results with associated uncertainties are tabulated in the Supplementary material. Modeling of the premixed free-propagating planar adiabatic flames was performed using ANSYS Chemkin 18 [38]. The solutions were tested for grid-independence. The number of grid points was typically 750–850.

## 3. Kinetic modeling and DFT analysis

### 3.1. Computational details

All calculations were performed using Gaussian 16 [39]. The ground state and transition state structures were optimized using the B3LYP/6-31G(df,p) level of theory. Structures were confirmed to be minima or transition states by the absence or presence of one imaginary frequency. Intrinsic reaction coordinate calculations confirmed that the transition states connected the appropriate reactant and product geometries. Energy calculations were performed using the G4 composite method on all optimized reactant, product, and transition state geometries [40]. The G4 composite method has previously been benchmarked against various computational methods and shown to compute accurate dissociation energies for open- and closed-shell systems (1.08 and 1.48 kcal mol<sup>-1</sup>, respectively) and transition state energy barriers [41–43]. The G4 energies at 1000 K and the kinetic parameters were computed using a modified version of GoodVibes [44]. To interpret the results from the microflow work at the VUV beamline, we calculate ionization energies, equilibrium structures, and vibrational modes of intermediates and products at B3LYP/6-311++G(d,p). Adiabatic ionization energies were refined by optimizing the neutral and ion state of the desired molecule and considering the zero-point energy at the CBS-QB3 level of theory. Photoion mass-selected threshold photoelectron spectra were analyzed using either reference spectra or a Franck-Condon approach as implemented in eZpectrum [45] or Gaussian16, to assign *m/z* peaks in the mass spectrum isomer-selectively. The stick spectra were convoluted with a Gaussian function to account for the rotational envelope of each vibrational band and compared with the experimental spectrum.

The location of the weakest C–C and C–H bonds and the resulting radical fragments give a first insight into the high-temperature combustion reaction pathways. At high combustion temperatures ( $\geq$ 1100 K), unimolecular dissociation and radical bimolecular hydrogen abstraction reactions are expected to be prominent. Computing the bond dissociation enthalpies (BDE) for the two isomers will identify the initial combustion reactions at elevated temperatures. The BDEs for DIB-1 and DIB-2 are presented in Fig. 1, and the weakest bonds for DIB-1 and DIB-2 correspond to carbon–carbon (C–C) fission with similar BDEs (72 kcal mol<sup>-1</sup>). Additionally, the weakest C–H bonds were identified because these are assumed to be the most likely position for H-atom abstraction by a radical intermediate. The weakest C–H bond for both DIB-1 and DIB-2 is on the terminal primary carbon, alpha to the double bond due to the formation of resonance stabilized radical intermediates. This is expected for DIB-2; however, for DIB-1, the central secondary carbon has the weakest C–H BDE as determined by Yin et al. [17]. H-atom abstraction from the central carbon forming a radical will likely induce higher steric hindrance with the *tert*-butyl group than the radical formed on the terminal carbon. Therefore, the added steric contribution for the radical intermediate results in a higher BDE value for the central carbon vs. the primary carbon. The BDE trends presented here agree with the computed BDE trends by Terracciano et al. [10]. The next Sections 3.2 to 3.4 de-

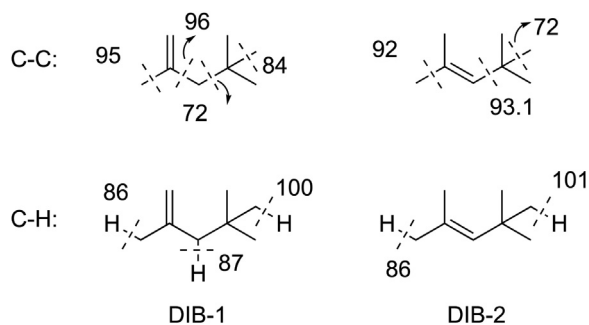


**Fig. 1.** Carbon–carbon and carbon–hydrogen bond dissociation enthalpies (BDE, in kcal mol<sup>-1</sup>) computed using the G4 composite theory at 298 K. Dashed lines indicate bond dissociation.

scribe how the rate constants for the high-temperature reactions classes were obtained for the chemical kinetic model.

### 3.2. Pyrolytic reactions

Unimolecular decomposition reactions involving C–C bond cleavage producing methyl and C<sub>7</sub> olefin tertiary radicals and retroene reaction producing two *iso*-butene molecules are adapted from [46] and [47], respectively. Other bimolecular channels are included assuming analogous pressure dependent rates calculated at CCSD(T)/cc-pVTZ level of theory on propene potential energy surface by Ye et al. [48]. The decomposition of DIB-1 forming 2-methyl allyl and *tert*-butyl radicals was described as an association reaction in the reverse direction using analogies from 1-butene chemistry.

### 3.3. H-atom abstraction reactions

The analogous propene rate constants were used for DIB primary allylic H-atom abstraction by H atoms and CH<sub>3</sub> radicals [49]. To simulate H-atom abstraction reactions from the secondary allylic site, respective 1-butene (C<sub>4</sub>H<sub>8</sub>-1) analogies were used [50–52]. The rate constants for abstraction from the primary hydrogen site were adopted analogously to *iso*-octane kinetics [53,54] since the presence of the C=C has no influence on this site. Comparison of C–H BDEs for the primary carbon of DIB-1 and DIB-2 (100.1 and 100.6 kcal mol<sup>-1</sup>, respectively) with *iso*-octane's primary carbon

C–H BDEs (100.5 and 100.6 kcal mol<sup>-1</sup>) [55], further justifies this adoption.

### 3.4. DIB radical decomposition reactions

The primary allylic (iC<sub>8</sub>D<sub>4</sub>-5R) DIB radicals decompose via β-scission to allene (C<sub>3</sub>H<sub>4</sub>-a) and *neo*-pentyl radical (neoC<sub>5</sub>H<sub>11</sub>), for which analogous iC<sub>4</sub>H<sub>7</sub> radical decomposition rates from Tranter et al. [56] were used. The β-scission reaction rate coefficients of primary (iC<sub>8</sub>D<sub>4</sub>-1R) radical and secondary allylic (iC<sub>8</sub>D<sub>3</sub>-5R) radical are taken from Wang et al. [46].

The detailed kinetic model including different reaction classes discussed in Part I, as well as thermodynamic and transport parameters and species dictionary are available as Supplementary material to Part I [1].

## 4. Results and discussion

### 4.1. Microflow reactor (PSI)

Since at high combustion temperatures, unimolecular reactions, such as C–C and C–H bond cleavage reactions of DIB-1 and -2, are becoming increasingly important, we investigated these reactions and compare them to the ones summarized in Fig. 1. We focus especially on the appearance of reactive and elusive molecules, which cannot be detected using conventional chemical analysis tools such as gas chromatography mass spectrometry (GC/MS). Due to the unavailability of reliable photoionization cross sections, our speciation data is based on relative mass signal levels and thus to be treated as semi-quantitative. Nevertheless, our data reveals unparalleled insights into the early stage of the high-temperature combustion mechanism, including detection of reactive radicals as a function of the reactor temperature. The decomposition reactions of DIB-1 (*m/z* 122, **1**) is investigated as a function of the reactor temperature by applying photoionization mass spectrometry (PIMS) at 10.5 eV photon energy. The semi-quantitative experimental species profiles as function of the reactor temperature are depicted in Fig. 2, and a selection of mass spectra are presented in the supporting information (Fig. S1). DIB-1 starts to decompose in the pyrolysis microreactor at around 800 K, with the appearance of reactive species at *m/z* 56 and 55. To assign isomers to the respective *m/z* values in the PIMS (Fig. 2), we utilized photoion mass-selected threshold photoelectron spectroscopy (ms-TPES), which has been shown to be a versatile tool to get isomer-

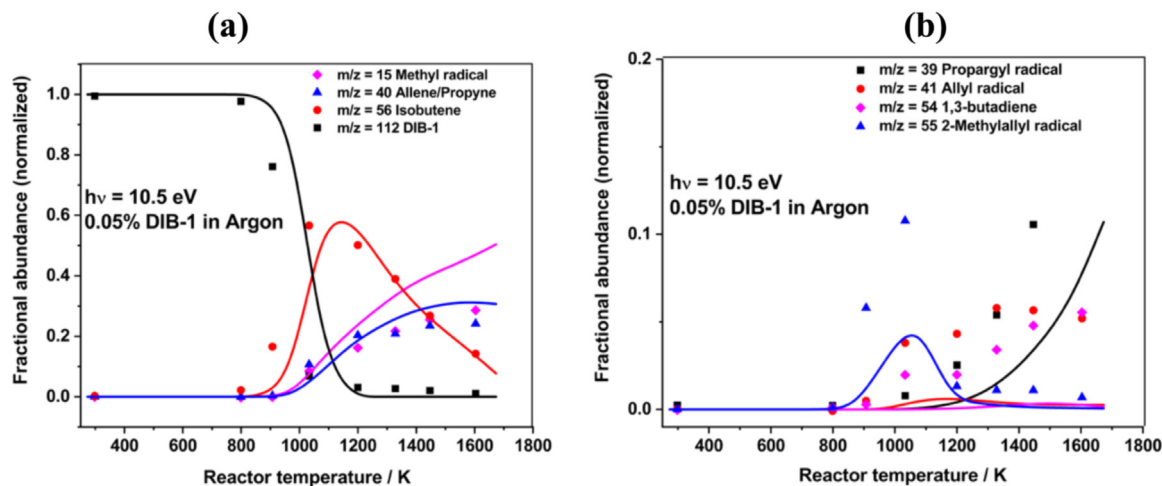


**Fig. 2.** Semi-quantitative temperature dependent species profiles measured during the thermal decomposition of DIB-1. Symbols: experiment, lines: model from this study assuming constant pressure and residence time of 15 mbar and 50 μs respectively covering temperatures from 300 to 1800 K. The fractional abundance is normalized based on the initial fuel concentration (see Table S3).

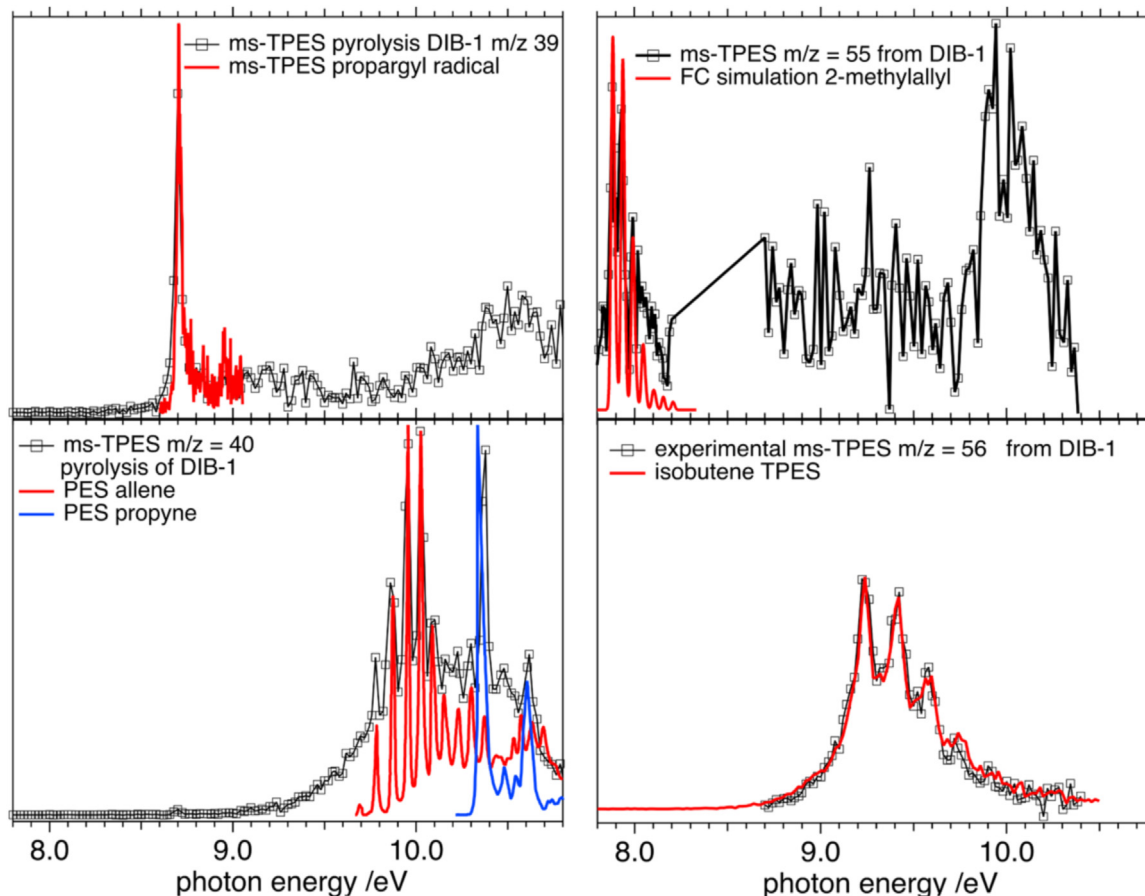


**Fig. 3.** Photoion mass-selected threshold photoelectron spectra (ms-TPES) of the intermediates and reaction products in the temperature range 975–1175 K. PES denotes photoelectron spectra from the literature. Species are isomer-selectively assigned using either Franck-Condon (FC) simulations or reference data (solid lines).

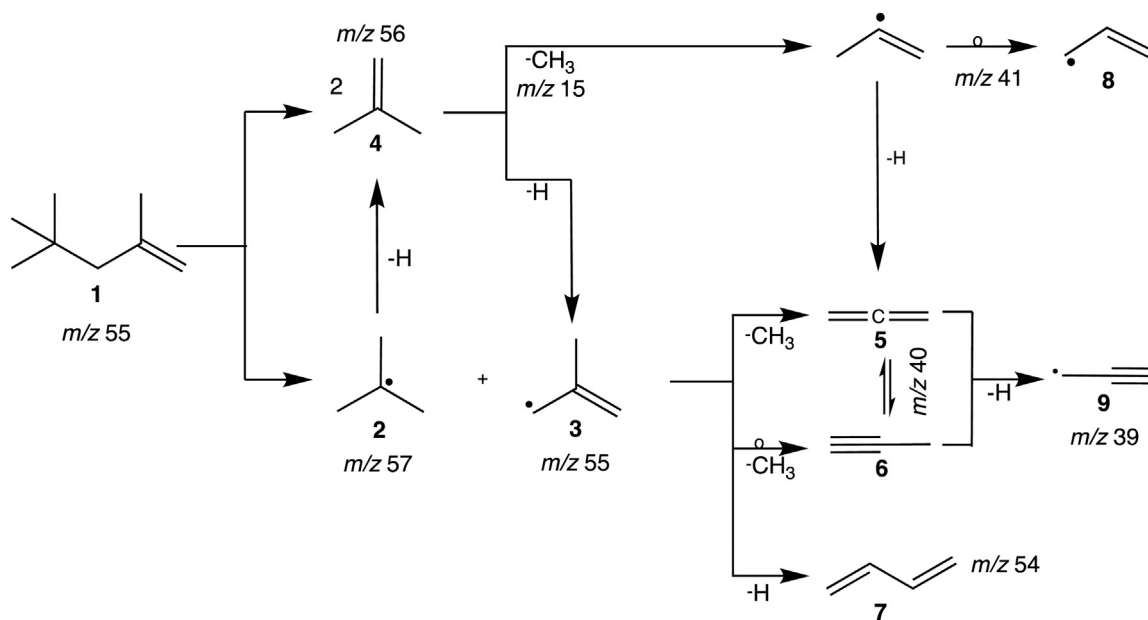


**Fig. 4.** Reaction mechanisms of the DIB-1 decomposition at unimolecular pyrolytic conditions. The fuel destruction is initiated by either a  $tC_4H_9$  (2,  $m/z$  57) and  $iC_4H_7$  (3,  $m/z$  55) radical formation or by hydrogen transfer from the  $CH_3$  groups to yield *iso*-butene (4).

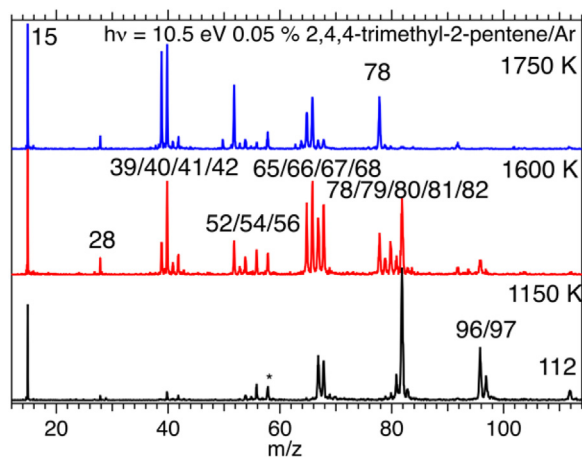


**Fig. 5.** Mass spectra of the decomposition of DIB-2 taken at 10.5 eV photon energy at varying pyrolysis temperature. The species assignments, based on the ms-TPES, can be found in the text.

specific data in kinetics and flame experiments, by comparing the experimental spectrum to reference or Franck-Condon simulated ones [57,58]. Fig. 3. reveals, the formation of *iso*-butene ( $m/z$  56, **4**) and 2-methylallyl radicals ( $m/z$  55,  $i\dot{C}_4H_7$ , **3**), in the reaction mixture (see Figs. 2 and 3)(Bold numbers are used later in Fig. 4). In addition, we find traces of *tert*-butyl radicals ( $m/z$  57,  $t\dot{C}_4H_9$ , **2**) especially at low reactor temperatures, however, due to the lability of the C–H bond, the radical rapidly decomposes in a hydrogen loss reaction to form *iso*-butene, which is in agreement with the lowest C–C bond dissociation energy ( $71.8 \text{ kcal mol}^{-1}$  at 298 K) in Fig. 1. At higher photon energies and 800 K reactor temperature, dissociative ionization of DIB-1 sets in, giving rise to  $m/z$  57 fragments, which were added to the parent signal. A reference spectrum of DIB-1 without pyrolysis can be found in Fig. S1. Due to the high abundance of *iso*-butene, DIB-1 can undergo also a retro-ene rearrangement reaction, where the hydrogen of the *tert*-butyl group is shifted to the  $CH_2$  group in the center of the molecule affording two equivalents of *iso*-butene. Thus, the initial fuel decomposition channel of DIB-1 at unimolecular conditions is a branching yielding either  $t\dot{C}_4H_9$  (**2**,  $m/z$  57) and  $i\dot{C}_4H_7$  (**3**,  $m/z$  55) radicals or *iso*-butene (Fig. 4,  $m/z$  56). This result is in agreement with the weakest BDE calculated for DIB-1 (Fig. 1).

At reactor temperatures as high as 1200 K, 2-methyl allyl ( $i\dot{C}_4H_7$ ) radical (**3**,  $m/z$  55) vanishes, while the  $C_3H_4$  ( $m/z$  40), methyl radical ( $m/z$  15), and  $C_4H_6$  ( $m/z$  54) signals increase. Ms-TPE spectra verify that both  $C_3H_4$ -a (**5**,  $m/z$  40) and  $C_3H_4$ -p (**6**,  $m/z$  40) contribute to the signal at  $m/z$  40 (Fig. 3), while 1,3-butadiene (**7**,  $m/z$  54) and hydrogen atoms are also produced in small quantities. These reactions were confirmed by pyrolyzing 3-bromo-2-methylpropene (see Supplementary material), which is a well-known precursor for  $i\dot{C}_4H_7$  (**3**,  $m/z$  55), yielding also the previously mentioned products, as summarized in Fig. 4. *iso*-butene ( $m/z$  56, **4**) is one of the major products, but it slowly decreases at around 1000 K, Fig. 2(a), while allyl radicals ( $m/z$  41, **8**,  $\dot{C}_3H_5$ -a) are generated by methyl radical loss and a rearrangement reaction as shown in Fig. 4 and verified by pyrolysis measurements of plain *iso*-butene (see Supplementary material). Allyl radicals are also prone to hydrogen loss to produce allene **5** and propyne **6** (both  $m/z$  40) and, thus, also contribute to  $m/z$  40. Another hydrogen loss yields propargyl ( $\dot{C}_3H_3$ ,  $m/z$  39, **9**) radicals [59].

In DIB-2, the double bond is shifted towards the center of the molecule compared to DIB-1, which results in a large number of feasible decomposition pathways yielding multiple fragments, presented in Fig. 5. Thus, DIB-2 fuel destruction pathways are more complex than those of DIB-1. The fuel decomposition starts at

around 800 K (see Fig. 6), where we observe methyl radicals at  $m/z$  15,  $C_5H_{7/8}$  ( $m/z$  67, 68),  $C_6H_{9/10}$  ( $m/z$  81, 82) and  $m/z$  96 and 97 from  $C_7H_{12/13}$  species. Above 1400 K, further decomposition channels open up, which can be assigned to ethylene ( $m/z$  28), propargyl ( $m/z$  39), allene, propyne ( $m/z$  40), allyl ( $m/z$  41), along with  $C_4$  ( $m/z$  52–56) and  $C_5H_6$  ( $m/z$  66) species. More insight on the reaction mechanism and the parallel and sequential reactions can be obtained by plotting the reactor temperature dependent species profiles, as depicted in Fig. 6. It is evident that closed shell species such as  $m/z$  82 ( $C_6H_{10}$ ), 96 ( $C_7H_{12}$ ), and 68 ( $C_5H_8$ ) are formed in parallel with methyl radicals ( $m/z$  15). A large signal at  $m/z$  97 is also observed at 1150 K in Fig. 5. We may be tempted to assign this to the  $\dot{C}_7H_{13}$  radical formed after initial methyl radical loss. However, close inspection of this fragment utilizing cation velocity map imaging revealed a broad velocity distribution of this cation perpendicular to the molecular beam, which indicates kinetic energy release in cation fragmentation. In addition, a reference ms-TPES of the un-pyrolyzed DIB-2 is given in Fig. S4j, which shows the appearance of  $m/z$  97 at ca. 10 eV. Therefore, it is in fact formed by dissociative ionization of DIB-2 at elevated reactor temperatures, as pointed out recently [60]. Above 1300 K reactor temperature, the signal of the closed shell species  $C_6H_{10}$  ( $m/z$  82),  $C_7H_{12}$  ( $m/z$  96), and  $C_5H_8$  ( $m/z$  68) degrade again (Fig. 6) to yield secondary products such as  $C_6H_8$ ,  $C_6H_6$ ,  $C_5H_6$ ,  $C_5H_5$ ,  $C_4H_4$ , and  $C_3H_4$ . Propargyl radicals ( $\dot{C}_3H_3$ ) are observed at the highest reactor temperatures.

Photoion mass-selected threshold photoelectron spectroscopy (Fig. 7) was applied to assign reactive intermediates and stable products isomer-selectively for each mass channel. While for smaller fragments only a few isomers exist, the spectra are not discussed in detail here, but they are presented in the Supplementary material (Fig. S4) together with reference spectra or Franck-Condon simulations to prove their identity. We assigned  $m/z$  15, 28, 39, 40, 41, 42, 52, and 54 to methyl, ethylene, propargyl, allene/propyne, allyl radicals, propene, vinylacetylene, and 1,3-butadiene/2-butyne, respectively. Despite the precursor being acyclic, we also identify five- and six-membered rings, such as cyclopentadienyl ( $m/z$  65), cyclopentadiene ( $m/z$  66), fulvene ( $m/z$  78) and benzene ( $m/z$  78) in unimolecular conditions. The spectra of the remaining species are depicted in the Supplementary material (Fig. S4).

As indicated by the species profiles in Fig. 6, we observe depletion of the fuel at around 950 K, while intermediates of the composition  $C_5H_8$  ( $m/z$  68),  $C_6H_{10}$  ( $m/z$  82) and  $C_7H_{12}$  ( $m/z$  96) arise together with a methyl radical.

Thus, DIB-2 (**10**) decomposition is initiated by fission of the weakest C–C bond (Fig. 1,  $71.1 \text{ kcal mol}^{-1}$  at 298 K) resulting in a demethylation reaction yielding tetramethyl allyl radicals **11** ( $m/z$  97), which are subject to three branching reactions as depicted in Fig. 8. The tetra-methyl allyl radical (**11**) can be stabilized by further hydrogen atom loss to yield 2,4-dimethyl-1,3-pentadiene **12** (I24C7D13,  $m/z$  96). The experimental ms-TPE spectrum of  $m/z$  96 is depicted in Fig. 7 and shows good agreement with the Franck-Condon simulation of I24C7D13. The calculated adiabatic ionization energy at 8.25 eV (CBS-QB3) also agrees well with the first feature of the spectrum. We have evaluated further 12 different  $C_7H_{12}$  isomers (see Supplementary material, Table S1,  $m/z$  96) with six- and five-membered ring species, but the agreement of the calculated IE and the Franck-Condon envelope was not satisfying.

Besides the previously mentioned hydrogen loss, tetra-methyl allyl **11** can formally lose a methyl group to yield isomers of the composition  $C_6H_{10}$  ( $m/z$  82, **13**). Ionization energies and Franck-Condon simulations have been performed for 15 different isomers. Amongst the cyclic species, only 1-methylcyclopentene fits in the spectral energy range of the TPES (see Fig. 7). However, up to ten  $C_6$  species ionize below 9 eV and may also be formed upon decomposition of DIB-2. We have fitted the experimental spectrum using the Franck-Condon simulation of E- and Z-2-methyl-



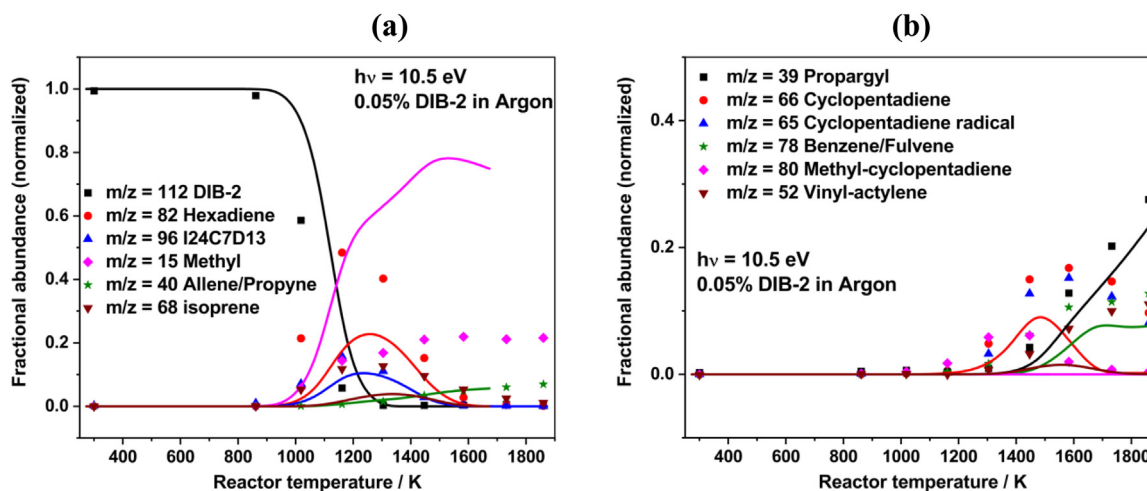


**Fig. 6.** Semi-quantitative temperature dependent species profiles measured during the thermal decomposition of DIB-2. Symbols: experiment, lines: modeling. Note that due to the absence of ionization cross sections for most of the species, we can only provide fractional signal abundances (see Table S4).

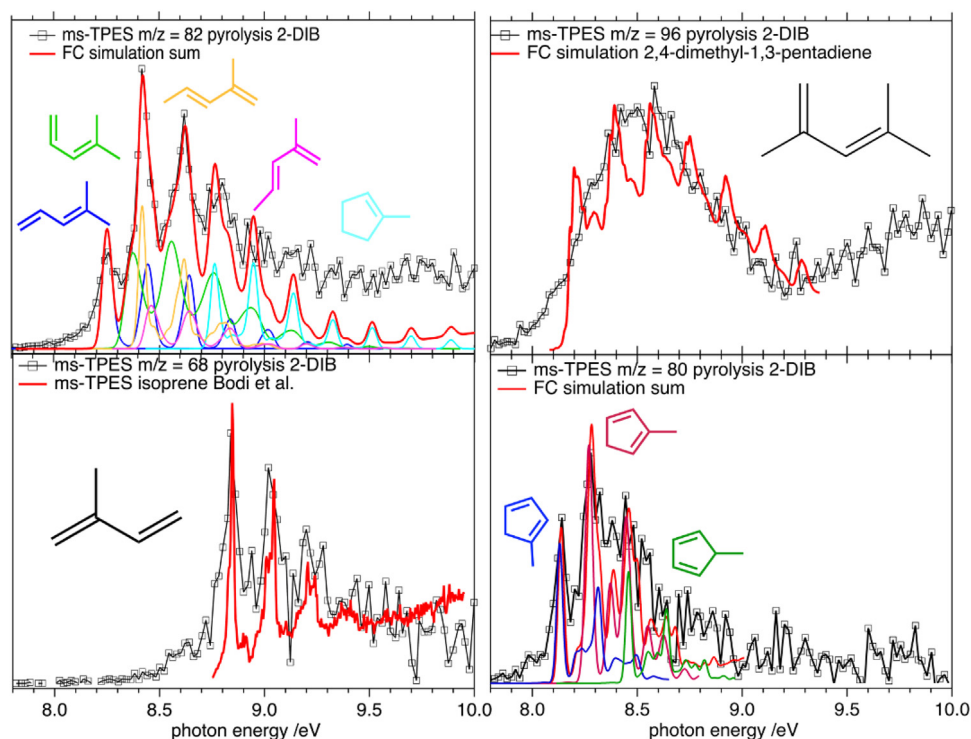


**Fig. 7.** Photoion mass-selected threshold photoelectron spectra of larger species appearing during the decomposition of DIB-2, as measured in a 1150–1500 K reactor temperature range. Reference spectra from [27,61].

1-3-pentadiene, E- and Z-4-methyl-1-3-pentadiene as well as 1-methylcyclopentene and a good agreement can be achieved. However, we cannot exclude contributions of other branched C<sub>4</sub>- or C<sub>6</sub>-chains. From a chemical perspective though, the formation of these isomers should involve multiple methyl migration steps, which are unlikely in these systems at unimolecular conditions.

The third parallel decomposition channel occurring at lower reactor temperatures is accompanied by a formal  $\dot{C}_2H_5$  loss and yields *m/z* 68. Since C<sub>5</sub>H<sub>6</sub> and  $\dot{C}_5H_5$  species are cyclic isomers, it would be obvious that the C<sub>5</sub>H<sub>8</sub> isomers are also cyclic, however, the spectrum of *m/z* 68 is dominated by isoprene **14** based on the comparison with its reference TPE spectrum. Due to the rather broad peaks, cyclopentene can however not be fully ruled out to also contribute to the spectrum. Ethyl radicals, however, are only observed in very low concentrations below 950 K reac-

tor temperature. Furthermore, ethyl radical abstraction would only be available after multiple rearrangement reactions and, in the absence of their products, it is deemed unlikely. The appearance of *m/z* 68, isoprene **14**, still has to be understood. The tetramethyl allyl radical **11** may be subject to a ring-closure reaction affording a dimethyl cyclopentanyl radical **15**, which can demethylate to form 3-methylcyclopentene **16** as observed in the ms-TPES in Fig. 7. However, branching is likely to occur and the five-membered ring in **15** may expand to a methyl cyclohexyl radical **17**. Hydrogen loss will probably yield three different methyl cyclohexene isomers (**18**, **19**, and **20**). The ms-TPES of *m/z* 96 did not show any indication for methyl cyclohexenes. Just recently, we found that retro-Diels–Alder reactions are typical pathways for the decomposition of 6-membered ring species at pyrolysis conditions [62]. Indeed, a retro-Diels–Alder (4 + 2 cyclo reversion) reaction of the

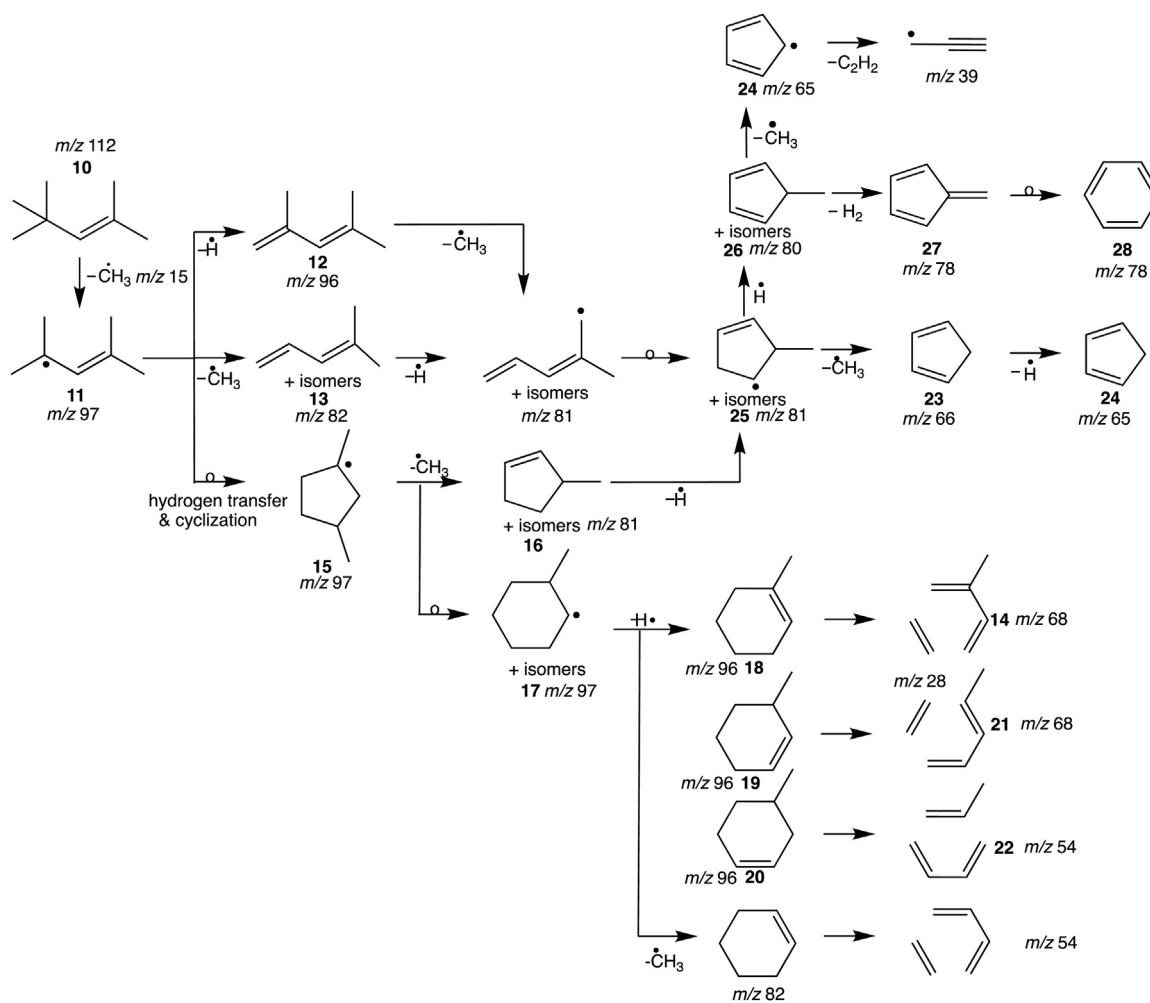


Fig. 8. Reaction mechanisms of the DIB-2 decomposition at unimolecular pyrolytic conditions.

methyl cyclohexenes (**18**, **19**, or **20**,  $m/z$  96) can explain the appearance of ethylene/isoprene **14**, ethylene/1,3-pentadiene (**21**), or propene/1,3-butadiene (**22**), according to Fig. 8. *Ab initio* branching ratios among the individual decomposition channels would require extensive quantum chemical exploration of the potential energy surface, which is beyond the scope of this manuscript. Nevertheless, pyrolysis microreactor experiments have revealed important details of the initial fuel destruction pathways of DIB-2. Further decomposition reactions of the intermediates can explain, e.g., the formation of cyclopentadiene **23** and cyclopentadienyl **24**, which is initiated via demethylation of the methyl-cyclopentenyl radical **25**. Methyl cyclopentadienes **26** ( $m/z$  80) are the precursors of fulvene ( $m/z$  78, **27**), also yielding benzene ( $m/z$  78, **28**) at higher pyrolysis temperatures.

In Figs. 2 and 6, we present not only semi-quantitative experimental species profiles, measured during the thermal decomposition of DIB-1 and DIB-2, respectively, but also show a qualitative comparison to predictions of the present model. Our model does not account for the temperature or pressure gradient in the reactor. In addition, we used the measured reactor surface temperature of 300 to 1600 K without further correction. (Section 2). For modeling the current experiments we assumed a constant pressure of 15 mbar and a residence time of 50  $\mu$ s, with temperature varying from 300 to 1800 K. Furthermore, as pointed out in Section 2.1, the fractional abundances from mass spectrometric signals need renormalization using the photon energy and species-dependent photoionization cross section, which are unavailable for many early

intermediates and products detected in this study [63]. Thus, our approach used here can be seen as semi-quantitative. Nevertheless, the decomposition of DIB-1 and the formation of major products, such as *iso*-butene, allene/propyne and methyl radicals shown in Fig. 2(a) are well captured by the present model mechanism. In the case of DIB-2, the difference between the measurements and modeling is somewhat higher, up to a factor of two for the major products Fig. 6(a). The variation of the key intermediates, such as hexadiene, I24C7D13 and isoprene with temperature is in qualitative agreement with experiments, thus substantiating fuel destruction pathways at pyrolytic conditions shown in Figs. 4 and 8. In summary, our semi-quantitative and isomer-selective approach reveals the initial C-C bond cleavage reaction triggering the high temperature combustion chemistry of both DIB-1 and -2. In addition, we obtained a comprehensive reaction mechanism specifying the fate of the first fuel radicals, *tert*-butyl and 2-methyl allyl in case of DIB-1 and methyl and tetramethyl-allyl for DIB-2.

#### 4.2. Flow reactor (NREL)

Flow reactor results in comparison to the DIB model in this study, are presented in Fig. 9(a–e) for  $\varphi = 1$  and Fig. 10(a)–(e) for  $\varphi = 3$ . In general, consumption of the parent DIB-1 and DIB-2 is well captured by the model for both isomers. As was observed in other studies [5,10], the formation of *iso*-butene is observed in significantly higher concentrations for DIB-1 versus DIB-2 at both equivalence ratios. This is also supported by DFT analysis (Fig. 1)

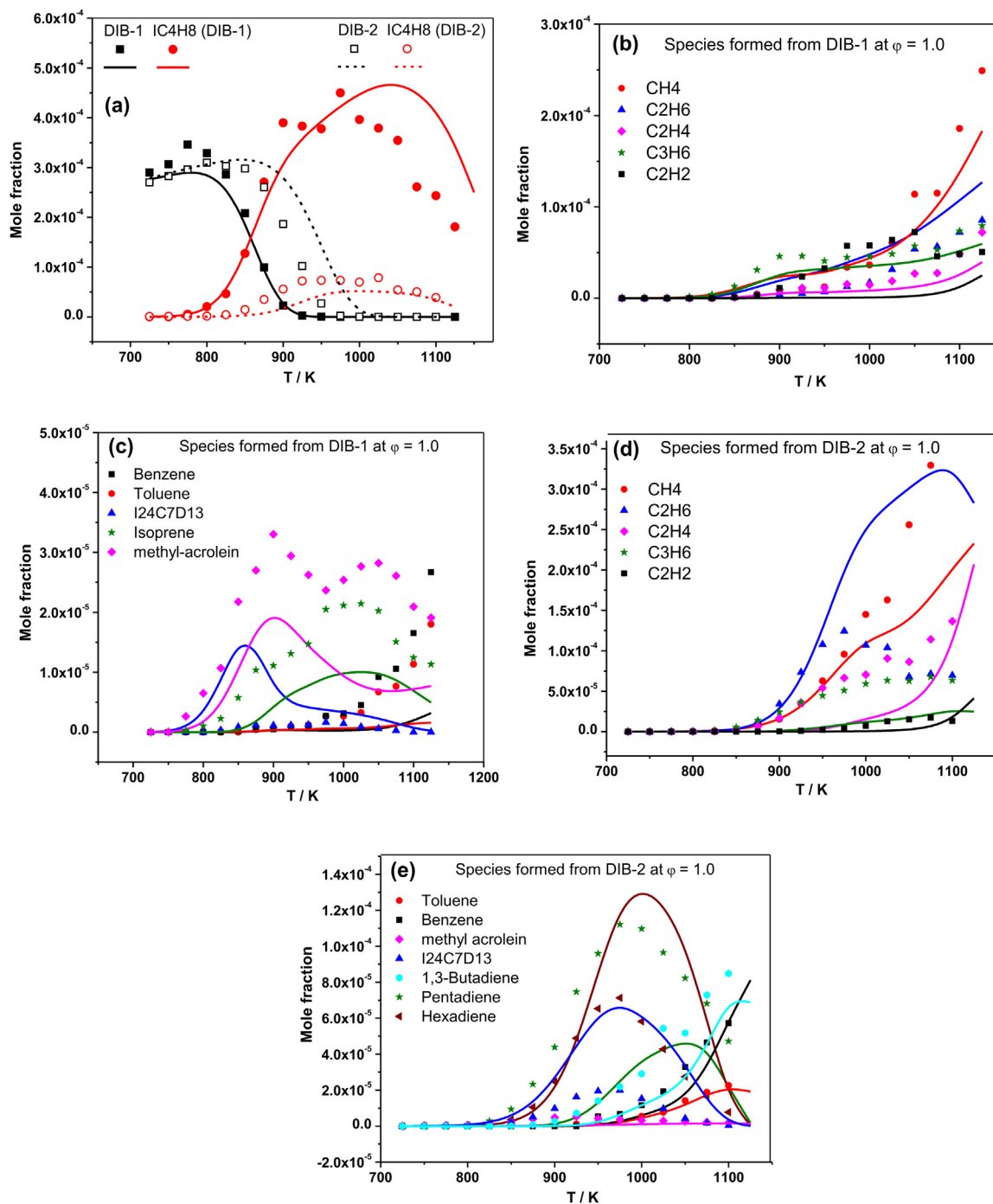


**Fig. 9.** Flow reactor analysis at  $\phi = 1.0$  and 0.85 atm with a residence time of 0.22 s for (a) the consumption of DIB isomers and formation of *iso*-butene from both isomers, (b) formation of C<sub>1</sub>-C<sub>3</sub> species from DIB-1, and (c) other major products formed from DIB-1, (d) formation of C<sub>1</sub>-C<sub>3</sub> species from DIB-2, and (e) other major products formed from DIB-2, across the temperature range of 725–1125 K.

and pyrolysis microflow reactor results which shows that DIB-1 mainly dissociates into C<sub>4</sub> fragments leading to *iso*-butene products, while DIB-2 mainly forms I24C7D13 Figs. 9(e) and 10(e). At an equivalence ratio of 1, benzene and toluene formation both are under-predicted by the model for DIB-1 but are well captured for the DIB-2 isomer. For the DIB-2 isomer, ethane at high temperature is over-predicted while the methane is under-predicted. In Fig. 10(b), the C<sub>1</sub>-C<sub>3</sub> species are well captured by the model, except for the formation of acetylene. For the DIB-2 isomer, several of the C<sub>1</sub>-C<sub>3</sub> species predictions are poor, especially above 950 K.

DIB-1 and DIB-2 we also examined at  $\phi = 3$  and at temperatures in the range 800–1100 K to simulate conditions more suscep-

tible to soot formation, Fig. 10. These conditions are more similar to those in the pyrolysis microflow reactor. In particular, the 5-fold excess of the benzene formation at  $\phi = 3$  in DIB-2, as compared to DIB-1, may be owed to the unimolecular fuel decomposition channels to benzene, observed in Fig. 8. Again, conversion of the parent compound and formation of *iso*-butene are well predicted, Fig. 10(a), with a much higher concentration of *iso*-butene being observed for the DIB-1 isomer, in-line with other studies [5,10]. This is also supported by the DFT analysis (Fig. 1). Another major product observed in flow reactor results was isoprene, which was underpredicted by the model for both DIB-1 and DIB-2. Isoprene was also detected in the microflow reactor for DIB-2 py-

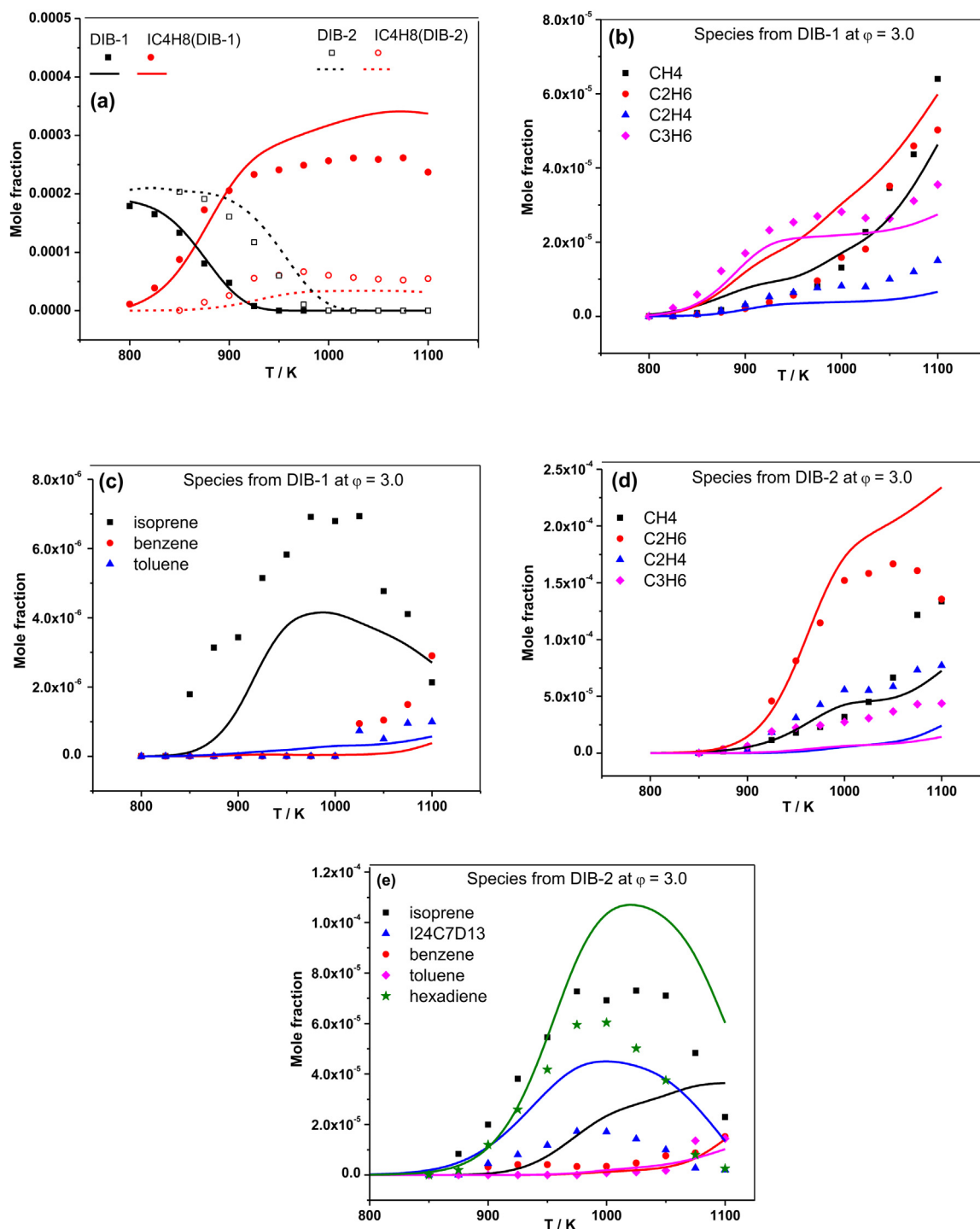


**Fig. 10.** Flow reactor analysis at  $\phi = 3.0$  and 0.85 atm with a residence time of 0.22 s for (a) the consumption of DIB isomers and formation of *iso*-butene from both isomers, (b) formation of C<sub>1</sub>–C<sub>3</sub> species from DIB-1, and (c) other major products formed from DIB-1, (d) formation of C<sub>1</sub>–C<sub>3</sub> species from DIB-2, and (e) other major products formed from DIB-2, across the temperature range of 800–1125 K.

rolysis, Fig. 5(b). Interestingly, hexadiene was measured in lower concentrations in the flow reactor than predicted by the model, Fig. 10(e), which seems to be in contradiction to the measurement-prediction for the microflow reactor results, Fig. 6, but could be due to uncertainties in the quantification.

#### 4.3. DFT analysis of high temperature reactions

A computational analysis was performed to gain further insight into the reaction pathways leading to the observed products for

DIB-1 and DIB-2. The reaction pathway analysis computed for DIB-1 is presented in Fig. 11. For comparison with the high temperature flow reaction analysis, all energies were computed at a temperature of 1000 K. The primary unimolecular dissociation reaction occurs with an energy barrier of 22.4 kcal mol<sup>-1</sup> forming two fragments, *iso*-butenyl (2-methyl-allyl) and *tert*-butyl radical. Hydrogen atom loss from the *tert*-butyl radical, or hydrogen addition to *iso*-butenyl radical forms *iso*-butene. *iso*-butene was the primary product detected in the flow reactor analysis for DIB-1 at both equivalence ratios (Figs. 9 and 10). Subsequent H-atom ab-

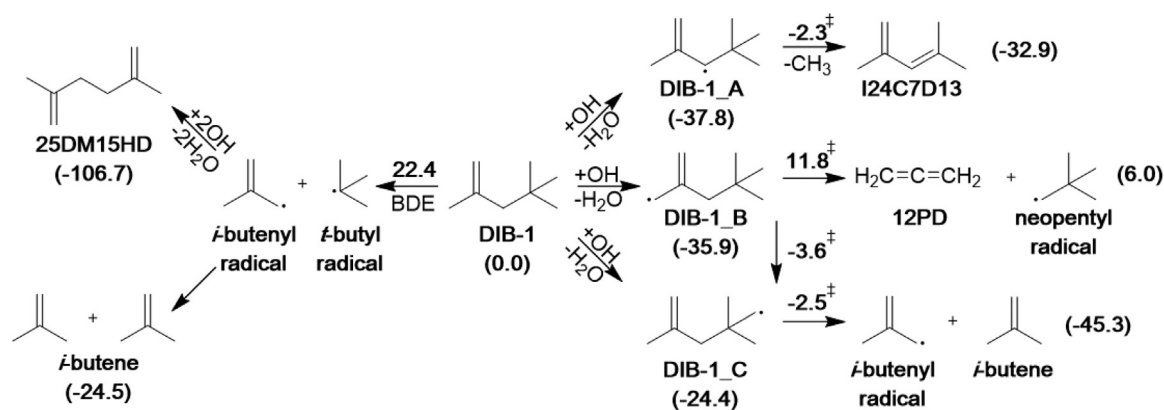


**Fig. 11.** Reaction diagram for DIB-1. Reactions are initiated by either C–C bond dissociation (left path) or bimolecular H-atom abstraction (right path). All energies are relative to the initial starting fuel, DIB-1, and presented in kcal mol<sup>-1</sup>, calculated using the G4 composite method at 1000 K. Energies in parentheses refer to the change in Gibbs free energies for the reaction, while energies with double dagger correspond to transition state energy barriers.

straction reactions from *iso*-butene and radical recombination of *iso*-butenyl radicals lead to the formation of 2,5-dimethylhexadiene (25DM15HD). This product was observed in the flow reactor analysis in low yields.

Bimolecular H-atom abstraction reactions are likely to compete with unimolecular dissociation. As shown in Fig. 11, three radical intermediates, DIB-1\_A, DIB-1\_B, and DIB-1\_C, can be formed following H-atom abstraction by a hydroxyl radical. Interestingly, the energetic trend determined for the three radical intermediates for DIB-1 does not match the trend predicted from the BDE analysis. This is due to the effect of entropy on the formation of the radical intermediates, which becomes more substantial at elevated ( $\geq 1000$  K) temperatures. Therefore, the second weakest C–H BDE results in the most favorable reaction pathway forming DIB-1\_A radicals. These react further by C–C dissociation forming 2,4-dimethyl-1,3-pentadiene (I24C7D13) with an energy barrier of 35.5 kcal mol<sup>-1</sup>. DIB-1\_B radicals react further via C–C fission, forming 1,2-propadiene and neopentyl radicals or via a H-shift isomerization forming DIB-1\_C radicals. The isomerization requires a lower energy barrier (32.2 kcal mol<sup>-1</sup>) compared to C–C bond fission (47.7 kcal mol<sup>-1</sup>); however it forms a less stable radical in comparison to DIB-1\_B. DIB-1\_C radicals, formed either via H-atom abstraction from DIB-1 or through isomerization from DIB-1\_B, dissociate further into *iso*-butenyl radicals and *iso*-butene with an energy barrier of 21.9 kcal mol<sup>-1</sup>. The primary penta- and hexadiene products formed through the bimolecular pathways (I24C7D13 and 25DM15HD) are observed in the flow reactor analysis in low yields, Figs. 9 and 10.

The analogous analysis was also performed for the high-temperature reaction pathways of DIB-2, presented in Fig. 12. Unimolecular dissociation of DIB-2 leads to a tetramethyl-substituted allyl radical, which, upon H-atom abstraction, can form I24C7D13. Further reactivity of this pentadiene product is of interest for soot precursor formation chemistry. Similarly, bimolecular H-atom abstraction reactions from DIB-2 lead to I24C7D13 through the radical intermediates, DIB-2\_B and DIB-2\_C. Lastly, DIB-2\_C radicals were found to have a second higher energy reaction pathway leading to *iso*-butenyl radicals and *iso*-butene. This reaction requires an energy barrier that is about 10 kcal mol<sup>-1</sup> higher than the path forming I24C7D13. The 2,4-dimethyl-1,3-pentadiene is expected to be the dominant product from the decomposition of DIB-2; however, low yields were observed in the high temperature flow reactor analysis. Therefore, it is assumed that at elevated temperatures, I24C7D13 reacts quickly, forming cyclopentadiene isomers and/or aromatic products.

This difference in reactivity and the sooting tendency for the DIB isomers is dependent on the chemical structure and the location of the double bond. DIB-1 mainly dissociates into C<sub>4</sub> fragments, leading to *iso*-butene products that delay and limit soot precursors (products containing one aromatic ring). DIB-2 primarily forms I24C7D13, which can easily undergo cyclization forming sootier aromatic products. Moreover, for comparison *iso*-butene contains a predicted yield sooting index (YSI) of 36.5 while I24C7D13 contains a predicted YSI of 65.4 [64]. Therefore, the I24C7D13 formation is the main contributor to the dramatic difference in the sooting tendency for the DIB isomers, which is already observed at unimolecular conditions as five and six-membered rings such as fulvene and benzene in the microflow reactor results.

#### 4.4. High-pressure shock-tube (NUIG)

The IDTs for DIB-1 were measured in the HPST (NUIG) at pressures and temperatures relevant to practical applications. The IDT data exhibited no negative temperature coefficient (NTC) behavior in the temperature range investigated and the logarithms of IDTs vary non-linearly with the inverse temperature, Fig. 13. The trends in the chemical kinetic model simulations agree well with the experimentally measured IDTs at 15 bar, Fig. 13(a) and 30 bar, Fig. 13(b). Quantitatively, the simulations are overall slow by 25–50% at 15 bar and agree well at 30 bar where most of the simulations are within the experimental error bars.

A flux analysis for DIB-1 was performed that shows the major reaction paths from the kinetic model ( $\phi = 1.0$  in air, at  $p = 30$  bar,  $T = 1200$  K and at 20% fuel consumed, Fig. 14). A high temperature of 1200 K was selected because of the focus of this paper and 30 bar because it is relevant for SI engine applications. The most important decomposition pathways of DIB-1 at 1200 K produce either *iso*-butene or its related radicals. The unimolecular decomposition reaction producing 2-methylallyl (*i*C<sub>4</sub>H<sub>7</sub>) and tert-butyl (*t*C<sub>4</sub>H<sub>9</sub>) radicals accounts for 36% of DIB-1 consumption, which agrees with the observation in the microflow reactor experiments and the DFT analysis discussed above. H-atom abstraction reactions at primary allylic and alkyl sites resulting in 12% and 20% of the fuel's consumption respectively. The fuel radicals formed mainly lead to the products *i*C<sub>4</sub>H<sub>8</sub> and *i*C<sub>4</sub>H<sub>7</sub>. H-atom addition reactions to the C=C double bond and a chemically activated channel contribute 7% and 3% of the fuel conversion to *iso*-butene and its radicals, respectively. At this condition, in total, about ~65% of DIB-1 consumption proceeds via the formation of *iso*-butene and hence it is a critical fragment in modeling the IDTs and LBVs of DIB-1.

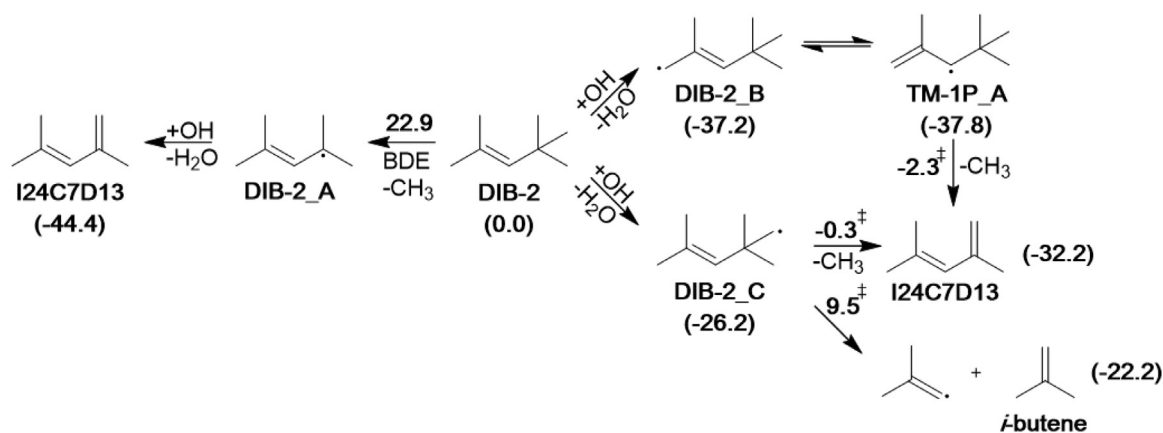


**Fig. 12.** Reaction diagram for DIB-2. Reactions are initiated by either C-C bond dissociation (left path) or bimolecular H-atom abstraction (right path). All energies are relative to the initial starting fuel, DIB-2, and presented in kcal mol<sup>-1</sup>, calculated using the G4 composite method at 1000 K. Energies in parentheses refer to the change in Gibbs free energies for the reaction, while energies with double dagger correspond to transition state energy barriers.

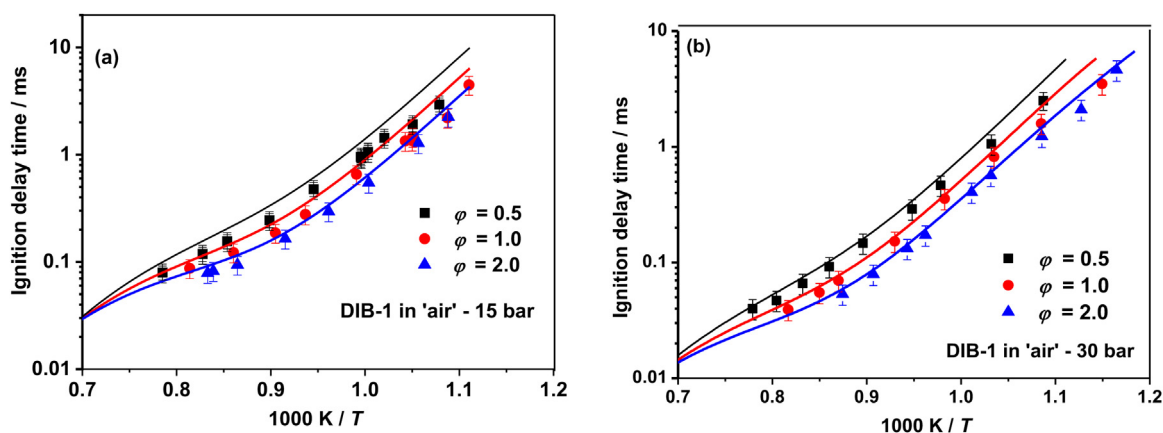


**Fig. 13.** The current model predictions for DIB-1 IDTs measured at NUIG HPST at  $\phi = 0.5, 1.0, 2.0$  fuel in air at 15 bar (a) and 30 bar (b).

Figure 15 depicts the controlling chemistry for DIB-1 IDT predictions at the same conditions as the flux diagram, Fig. 14, i.e., at  $\phi = 1.0$  in air,  $p = 30$  bar, and  $T = 1200$  K. Most of the sensitive reactions shown correspond to *iso*-butene chemistry and only two reactions correspond to DIB-1 chemistry. The unimolecular decomposition of DIB-1 ( $iC_8D_4 = tC_4H_9 + iC_4H_7$ ) significantly promotes the system's reactivity by the processes clearly observed under unimolecular conditions. Thus,  $iC_4H_7$  radicals react with  $HO_2$  and  $CH_3O_2$  radicals thereby converting less reactive radicals to relatively more reactive  $\dot{O}H$  and  $CH_3\dot{O}$  radicals, promoting reactivity. In addition, the recently updated cyclo-addition channel [65] of alkenyl peroxy radical ( $iC_4H_7O_2$ ) producing CCYCCOOC-t1 from ref. [66], promotes reactivity, since its decomposition pathways produce reactive species such as  $CH_2O$ ,  $CH_2CO$ ,  $HCO$  and  $\dot{C}H_3$  radicals. In addition, the small radical reactions,  $\dot{H} + O_2 = \dot{O} + \dot{O}H$ ,  $\dot{H} + O_2 (+M) = HO_2 (+M)$ , significantly promote reactivity. H-atom abstraction from the alkyl site on DIB-1 (forming  $iC_8D_4-1R$ ) inhibits reactivity, since it consumes  $\dot{H}$  atoms and eventually produces resonance stabilized radicals. The representative chain termination reactions,  $iC_4H_7 + \dot{C}H_3 = aC_5H_{10}$  and  $\dot{C}H_3 + HO_2 = CH_4 + O_2$  also reduce reactivity.

#### 4.5. Laminar burning velocities (Lund)

Figure 16 shows the laminar burning velocities of DIB/air flames measured in the present study, as well as DIB-1/air [15], and DIB-2/air [17] flames investigated in spherical flames at atmospheric pressure and at the unburned gas temperatures of 298 K. Asso-

ciated uncertainties of the present measurements, determined following the procedures presented by Alekseev et al. [37], are shown in Fig. 16 and other figures as error bars. The major factors contributing to the total uncertainties are the scatter in the recorded temperature profiles of the burner plate and uncertainty in the flow rates. The latter also determines the uncertainty in the equivalence ratio, presented in Fig. 16 with horizontal error bars. The overall accuracy is typically  $\pm 0.5$ – $1.0$  cm s<sup>-1</sup>, worse in rich mixtures. The burning velocities of DIB-2/air flames reported by Yin et al. [17] are slightly higher than those of DIB-1/air flames reported by Hu et al. [15], while the present measurements are close to these two datasets within the overlapping experimental uncertainties. Also shown in Fig. 16 are predictions of the mechanism developed in the present study for DIB/air flames, which are in good agreement with the measurements especially in lean and stoichiometric mixtures.

Figure 17 presents all the measurements performed in the present work at initial temperatures of 298, 318, 338, and 358 K. The present model nicely reproduces the shape of the  $S_L$  vs.  $\phi$  curve, as well as the trend of increasing burning velocities at higher temperatures. Four temperatures at each equivalence ratio allow for data consistency analysis similar to that performed for methylcyclohexane/air flames [67]. The temperature dependence of the laminar burning velocity can be interpreted using an empirical expression  $S_L = S_{L0} (T/T_0)^\alpha$ , assuming constant pressure, see Eq. (1), as it was demonstrated in many flame studies [11]. Thus, in log-log scale,  $S_L$  vs. temperature should obey linear trends at each equivalence ratio, as illustrated in Figs. 18 and 19 for lean and rich

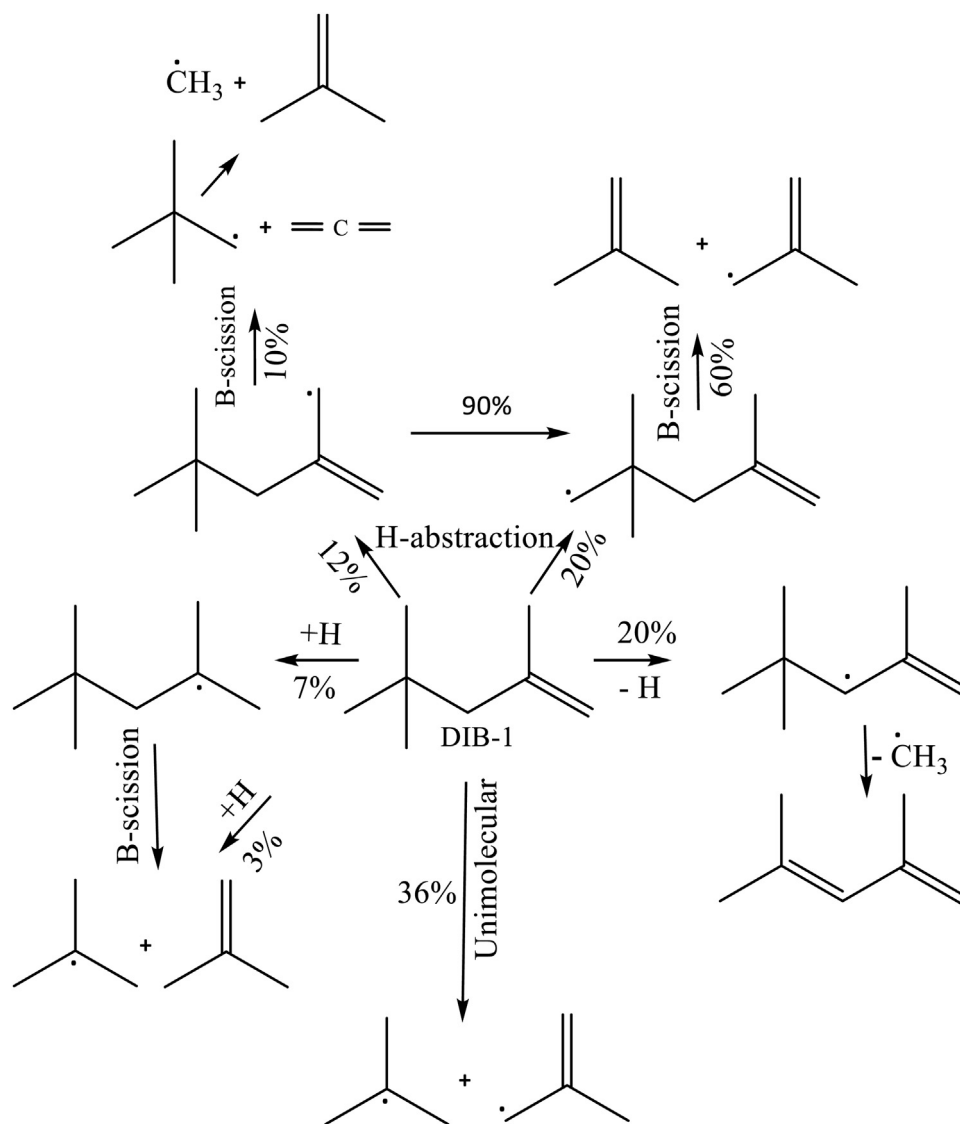


**Fig. 14.** Flux analysis using the current model for DIB-1 at  $\phi = 1.0$  in air, 30 bar at 1200 K and 20% fuel consumption, proceeds via various pathways producing *iso*-butene and/or its related radicals.

flames, respectively. Indeed, the present measurements shown as small symbols accurately follow the empirical expression for all  $\phi$ . The trendlines based on these results are extrapolated to the highest temperatures visited in the literature and all available data for DIB, DIB-1, and DIB-2 are also shown.

In stoichiometric mixtures, shown in Fig. 18, the results of Albright et al. [12] agree with the trendline only at the lowest temperature of their study (377 K), while, at higher temperatures, they systematically deviate from the expected dependence. Therefore, they concluded that the variation of the di-isobutylene  $S_L$  with temperature is the lowest as compared to other hydrocarbons studied [12].

The burning velocities of DIB-1 and DIB-2 obtained in the same laboratory by Hu et al. [15] and Yin et al. [17], respectively, show better agreement with the trendlines for lean mixtures in Fig. 18. In rich mixtures presented in Fig. 19, the deviation increases mostly because the difference in the  $S_L$  of DIB-2 and DIB-1 increases at these conditions as was demonstrated by Yin et al. [17]. Note that the uncertainties of their measurements (not shown in Figs. 18 and 19 to avoid clutter) were about 1–3 cm/s and thus some deviation from the trendlines is expected. As men-

tioned above, the DIB studied in the present work is a 3:1 mixture of DIB-1 and DIB-2, if the burning velocity dependence on composition is monotonic one may expect that the burning velocities of di-isobutylene should be in-between the values obtained by Hu et al. [15] and Yin et al. [17], which is observed in the rich mixtures, Fig. 19.

The burning velocities of DIB-1/air flames measured by Zheng et al. [13] with an estimated uncertainty of 2% show mixed behavior when compared to the trendlines in Figs. 18 and 19. They better agree with the literature data and expected trends at 450 K, while at 400 K the deviation is much higher with the datapoints lying lower by 5–8 cm/s. The values presented in these figures were obtained by non-linear stretch correction [13], yielding consistently lower results compared to the linear one. Nevertheless, the relative difference between these two approaches is about the same at 400 and 450 K that indicates some inconsistency of the 400 K data of the study by Zheng et al. [13].

The LBV of DIB-1/air flames obtained by Laich et al. [21] at 428 K better agree with the trendlines in Figs. 18 and 19, though some datapoints, e.g., for  $\phi = 0.9$  and 1.4 are obvious outliers. It should be noted that the measurements [21] were performed at

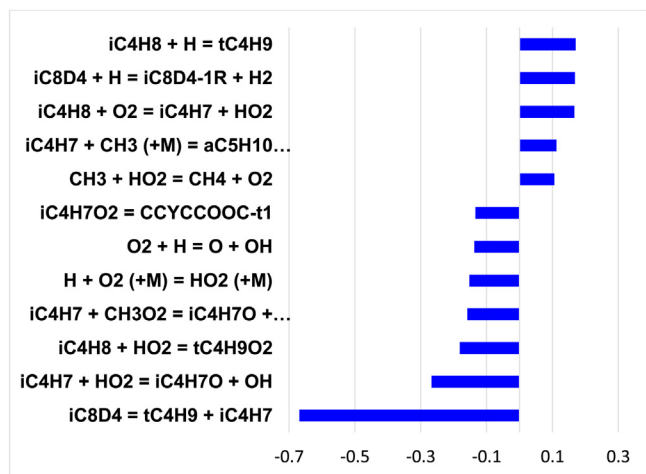


Fig. 15. Brute force sensitivity analysis representing reactions controlling DIB-1 IDTs using the new model at  $\phi = 1.0$  in air,  $p = 30$  bar, and  $T = 1200$  K.

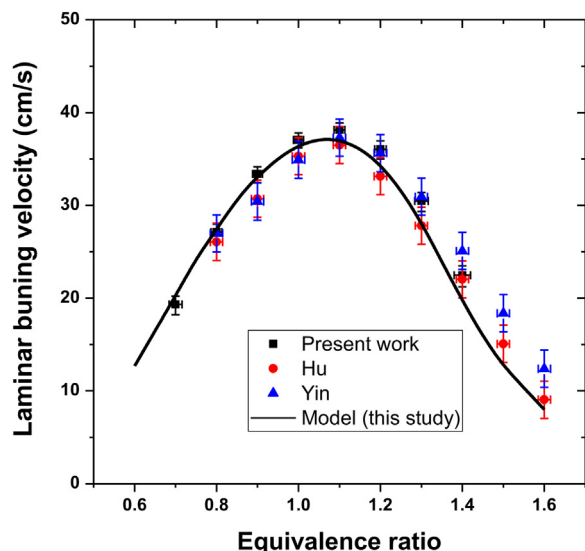


Fig. 16. Laminar burning velocity of DIB/air flames at 1 atm and initial temperature of 298 K. Symbols: experiments, line: modeling. Squares: DIB/air, present study, circles: DIB-1/air [15], triangles: DIB-2/air [17].

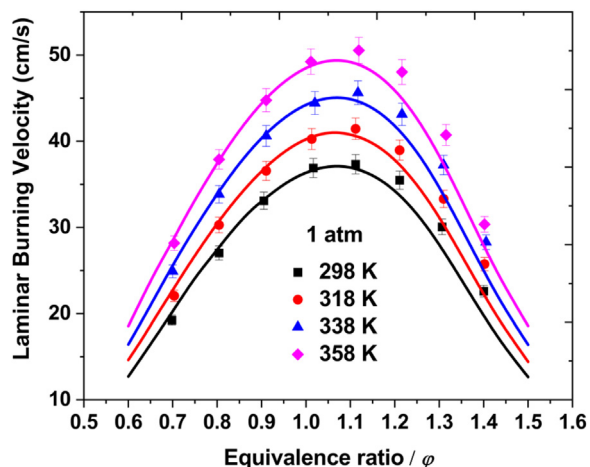


Fig. 17. Laminar burning velocity of DIB/air flames at 1 atm and initial temperatures of 298, 318, 338, and 358 K. Symbols: present experiments, lines: model predictions.

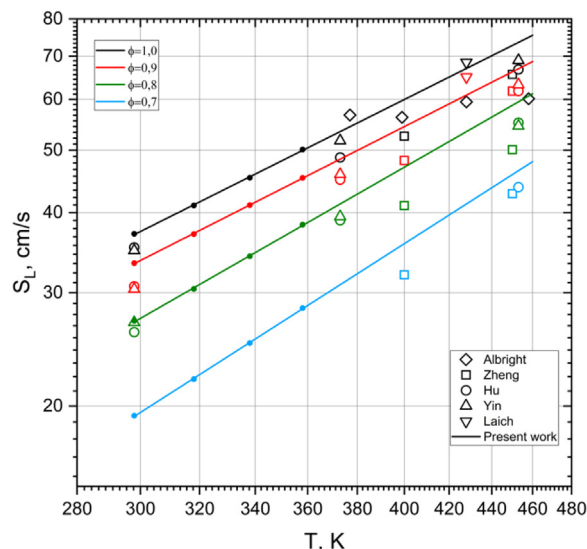


Fig. 18. Laminar burning velocity of lean and stoichiometric DIB/air flames at 1 atm and different initial temperatures. Symbols: experimental data, lines: trendlines based on the present measurements (solid symbols).

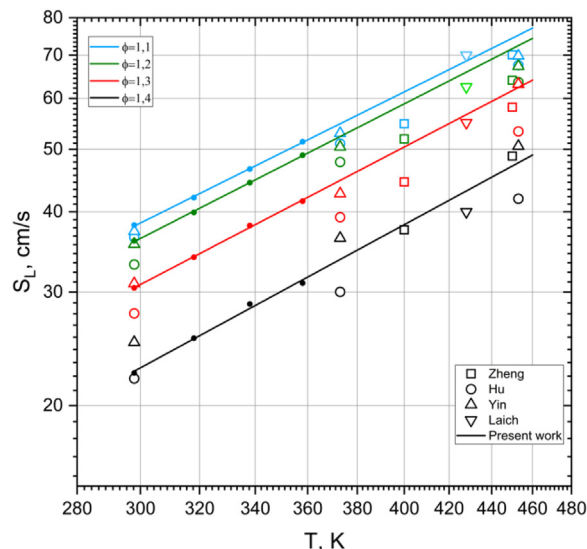


Fig. 19. Laminar burning velocity of rich DIB/air flames at 1 atm and different initial temperatures. Symbols: experimental data, lines: trend lines based on the present measurements (solid symbols).

equivalence ratios slightly different from the specific values shown in these plots; for example the maximum LBV of 70 cm/s was found at  $\phi = 1.08$ .

The slope of each trendline shown in Figs. 18 and 19 in log-log scale yields the power exponents  $\alpha$ , see Eq. (1). Temperature power exponents for hydrocarbons usually have moderate dependence on the equivalence ratio with a minimum in the mixtures possessing maximum burning velocity [11]. The power exponents  $\alpha$  of DIB/air flames at atmospheric pressure derived from the present experimental data as well as from the studies of Albright et al. [12], Zheng et al. [13], Hu et al. [15] and Yin et al. [17] are presented in Fig. 20. A linear least-square fit in logarithmic coordinates [68] was used to derive the power exponents  $\alpha$  and their uncertainties shown in this plot as error bars. Conforming with the previous discussion, the variation of the LBV observed by Albright et al. [12] contradicts other studies. The power exponents  $\alpha$  derived from the study by Zheng et al. [13] are systematically



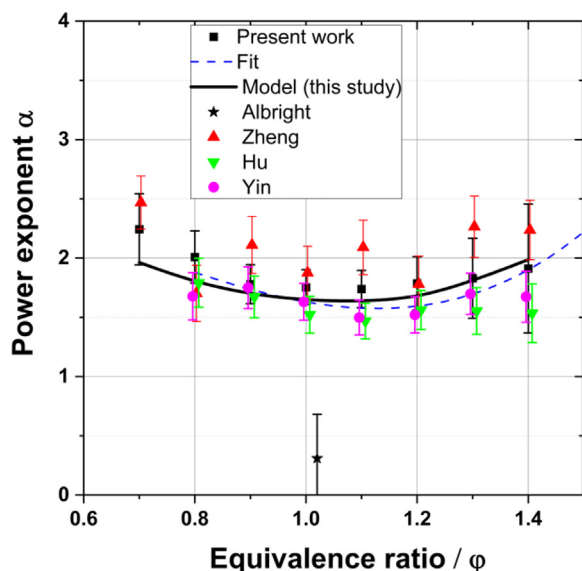


Fig. 20. Power exponent  $\alpha$  of DIB/air flames at atmospheric pressure. Symbols: present measurements, solid line: predictions of the present kinetic model, dashed line – empirical expression [15].

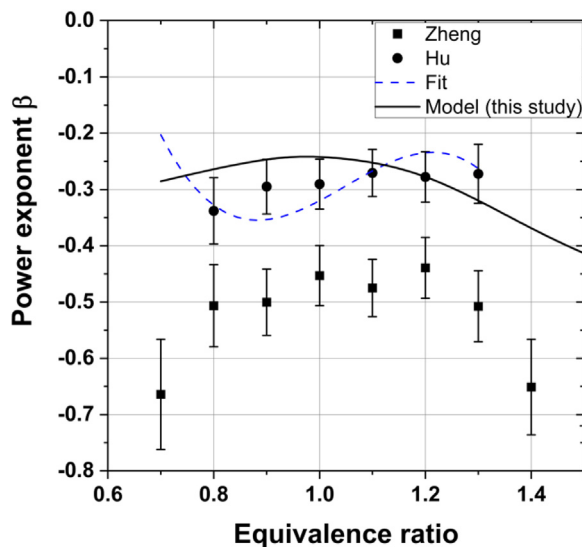


Fig. 21. Power exponents  $\beta$  of DIB-1/air flames. Symbols: derived from the measurements [13,15], solid line: predictions of the present kinetic model, dashed line – empirical expression [15].

higher than other datasets in Fig. 20, though within overlapping error bars reflecting lower than expected LBV values at 400 K as seen in Figs. 18 and 19.

The predictions of the present mechanism also shown in Fig. 20 are in good agreement with our experimental results as well as with the power exponents  $\alpha$  resulting from the measurements of Hu et al. [15] and Yin et al. [17]. Hu et al. [15] interpreted their measurements of DIB-1/air flames at different temperatures and pressures using Eq. (1) and approximated the power exponents  $\alpha$  and  $\beta$  by polynomial functions of  $\phi$ . Their empirical expression for the temperature power exponent agrees with the present results as well, Fig. 20.

To analyze the data consistency in terms of the pressure dependence, the measurements of the DIB-1/air flames performed at 1 and 3 atm [13], and at 1, 3, and 5 atm [15] were interpreted using Eq. (1). The power exponents  $\beta$  derived using a linear least-square fit in logarithmic coordinates are shown in Fig. 21 and compared

with the predictions of the present mechanism for DIB-1 as well as with the polynomial expression suggested by Hu et al. [15]. In the absence of reported error bars, the uncertainties of the power exponents were evaluated assuming the uncertainty of the burning velocity of  $\pm 2$  cm/s at each equivalence ratio [13,15]. The two series of experimental data shown in Fig. 21 do not overlap. This indicates some inconsistency of these measurements and/or underestimated experimental uncertainties. Predictions of the present kinetic model shown in Fig. 21 substantiate the dataset by Hu et al. [15]. For the pressure power exponents, different models indeed predict different dependencies, however, the shapes of the  $\beta - \phi$  curves are often similar as demonstrated for many hydrocarbons [11]. One may conclude that the third-order polynomial expression [15] should be used with caution outside its range of validity as it may predict values of  $\beta$  which are too high in lean and too low in rich mixtures, even though this expression agrees with individual datapoints derived from their work within the equivalence ratio range from 0.7 to 1.3.

## 5. Conclusions

We have investigated the oxidation chemistry of the 2,4,4-trimethyl-1-pentene (DIB-1) and 2,4,4-trimethyl-2-pentene (DIB-2) in a multipronged experimental and theoretical approach. We started with the unimolecular fuel decomposition mechanism of in a pyrolysis microreactor. The products and reactive intermediates, such as radicals, were isomer-selectively detected using VUV synchrotron radiation and photoelectron photoion coincidence techniques. Although DIB-1 and DIB-2 only differ in the position of the double bond, the fuel destruction pathways are markedly different. DIB-1 breaks at the central C-C bond affording 2-methylallyl and tert-butyl radicals, which rapidly yield *iso*-butene. The individually observed intermediates decompose further and can explain the appearance of allyl, allene, propyne, the methyl radical, etc. DIB-2 decomposition yields multiple products and is initiated by a methyl radical loss reaction, affording tetra-methyl allyl radicals as primary intermediates. Tetra-methyl allyl radicals decompose further through three different reaction channels. Interestingly, ring closure reactions to 5- and 6-membered ring species are observed and explain the formation of soot-precursors such as cyclopentadienyl, fulvene and benzene. These intermediates are, in general, responsible for PAH formation and are not found in DIB-1.

Oxidative experiments in a flow reactor at different equivalence ratios also show a five-fold higher propensity towards benzene formation for DIB-2 as compared to DIB-1, which can explain the increased sooting tendency, and is in line with the unimolecular reaction data.

In addition, to study the decomposition under inert and oxidative conditions, this work presents wide range of experimental IDT measurements for DIB-1, a gasoline surrogate fuel, which can be a direct validation target of the multi-component surrogate models featuring DIB-1. Our improved model can well capture the global reactivity targets of DIB-1 such as LBVs and IDT behavior from low to high temperatures at various conditions. The prominence of *iso*-butene chemistry to accurately model DIB-1 at high temperatures is highlighted via sensitivity and reaction pathway analyzes and is also found upon the unimolecular decomposition of DIB-1 in the microreactor. The kinetic analyzes of the DIB-1 reaction pathways performed at 1200 K show that the unimolecular decomposition to yield methyl-allyl and *tert*-butyl radicals dominates but also that hydroxyl (OH) radical addition and abstractions, by hydroperoxyl ( $\text{HO}_2$ ) and methyl peroxy ( $\text{CH}_3\text{O}_2$ ) radicals, are the major reason for promoting the reactivity at these conditions.

New measurements of the laminar burning velocities of DIB/air flames are presented. Experiments have been performed using the heat flux method at atmospheric pressure and initial temperatures

of 298–358 K. Moreover, data consistency was assessed with the help of analysis of the temperature and pressure dependencies of the laminar burning velocity, which was interpreted using an empirical power-law expression. The predictions of the present kinetic mechanism were found in excellent agreement with the new measurements. The part II of our DIB study complements our dataset and provides new insights into the reactions dominating under high temperatures, which may aid the development of predictive combustion models used for biomass-derived fuels.

### Declaration of Competing Interest

The authors declare that they have no known competing financial interests or personal relationships that could have appeared to influence the work reported in this paper.

### Acknowledgments

This work was supported by the Knut and Alice Wallenberg Foundation through grant KAW2019.0084 COCALD, Sweden. The study was also supported by the grant from the Russian Science Foundation (project No. 22-779-10205). M.S., A.B and P.H acknowledge funding by the Swiss Federal Office of Energy (SI/501269-01). The pyrolysis measurements were carried out at the VUV beamline of the Swiss Light Source, located at Paul Scherrer Institute in Villigen (Switzerland). The work at LLNL was performed under the auspices of the U.S. Department of Energy (DOE) by Lawrence Livermore National Laboratory under Contract DE-AC52-07NA27344 and was conducted as part of the Co-Optimization of Fuels & Engines (Co-Optima) project sponsored by the DOE Office of Energy Efficiency and Renewable Energy (EERE). Work at the National Renewable Energy Laboratory was performed under Contract No. DE347AC36-99GO10337 as part of the Co-Optimization of Fuels & Engines (Co-Optima) project sponsored by the U.S. Department of Energy's Office of Energy Efficiency and Renewable Energy Bioenergy Technologies Office and Vehicle Technologies Office. The authors at NUI Galway recognize funding support from Science Foundation Ireland (SFI) via project numbers 15/IA/3177 and 16/SP/3829. The authors at CNRS Orléans recognize funding support from the Agence Nationale de la Recherche (ANR) via the Labex CAPRYSES (ANR- 11-LABX-006-01).

### Supplementary materials

Supplementary material associated with this article can be found, in the online version, at doi:[10.1016/j.combustflame.2022.112547](https://doi.org/10.1016/j.combustflame.2022.112547).

### References

- [1] N. Lokachari, G. Kukkadapu, H. Song, G. Vanhove, M. Lailliau, G. Dayma, Z. Serinyel, K. Zhang, R. Dauphin, B. Etz, S. Kim, M. Steglich, A. Bodi, G. Fioroni, P. Hemberger, S.S. Matveev, A.A. Konnov, P. Dagaut, S.W. Wagnon, W.J. Pitz, H.J. Curran. A comprehensive experimental and kinetic modelling study of di-isobutylene isomers: part 1, *Combust. Flame*, [10.1016/j.combustflame.2022.112301](https://doi.org/10.1016/j.combustflame.2022.112301).
- [2] D.J. Gaspar, B.H. West, D. Ruddy, T.J. Wilke, E. Polikarpov, T.L. Alleman, A. George, E. Monroe, R.W. Davis, D. Vardon, Top Ten Blendstocks Derived From Biomass For Turbocharged Spark Ignition Engines: Bio-blendstocks With Potential for Highest Engine Efficiency, Report Number: PNNL-28713, Pacific Northwest National Lab.(PNNL), Richland, WAUnited States, 2019 <https://www.osti.gov/servlets/purl/1567705>.
- [3] R.L. McCormick, G. Fioroni, L. Fouts, E. Christensen, J. Yanowitz, E. Polikarpov, K. Albrecht, D.J. Gaspar, J. Gladden, A. George, Selection criteria and screening of potential biomass-derived streams as fuel blendstocks for advanced spark-ignition engines, *SAE Int. J. Fuels Lubr.* **10** (2017) 442–460.
- [4] J.P. Szybist, S. Busch, R.L. McCormick, J.A. Pihl, D.A. Splitter, M.A. Ratcliff, C.P. Kolodziej, J.M. Storey, M. Moses-DeBusk, D. Vuilleumier, What fuel properties enable higher thermal efficiency in spark-ignited engines? *Prog. Energy Combust. Sci.* **82** (2021) 100876.
- [5] W.K. Metcalfe, W.J. Pitz, H.J. Curran, J.M. Simmie, C.K. Westbrook, The development of a detailed chemical kinetic mechanism for diisobutylene and comparison to shock tube ignition times, *Proc. Combust. Inst.* **31** (2007) 377–384.
- [6] M. Fikri, J. Herzler, R. Starke, C. Schulz, P. Roth, G.T. Kalghatgi, Autoignition of gasoline surrogates mixtures at intermediate temperatures and high pressures, *Combust. Flame* **152** (2008) 276–281.
- [7] E. Hu, G. Yin, Z. Gao, Y. Liu, J. Ku, Z. Huang, Experimental and kinetic modeling study on 2, 4, 4-trimethyl-1-pentene ignition behind reflected shock waves, *Fuel* **195** (2017) 97–104.
- [8] H. Li, Y. Qiu, Z. Wu, S. Wang, X. Lu, Z. Huang, Ignition delay of diisobutylene-containing multicomponent gasoline surrogates: shock tube measurements and modeling study, *Fuel* **235** (2019) 1387–1399.
- [9] G. Yin, E. Hu, Z. Gao, F. Yang, Z. Huang, Kinetics of H abstraction and addition reactions of 2, 4, 4-trimethyl-2-pentene by OH radical, *Chem. Phys. Lett.* **696** (2018) 125–134.
- [10] A.C. Terracciano, S. Neupane, D.M. Popolan-Vaida, R.G. Blair, N. Hansen, G.L. Vaghjiani, S.S. Vasu, Elucidating the differences in oxidation of high-performance  $\alpha$ - and  $\beta$ -diisobutylene biofuels via Synchrotron photoionization mass spectrometry, *Sci. Rep.* **10** (2020) 21776.
- [11] A.A. Konnov, A. Mohammad, V.R. Kishore, N.I. Kim, C. Prathap, S. Kumar, A comprehensive review of measurements and data analysis of laminar burning velocities for various fuel+ air mixtures, *Prog. Energy Combust. Sci.* **68** (2018) 197–267.
- [12] R. Albright, D. Heath, R. Thena, Flame velocities of liquid hydrocarbons, *Ind. Eng. Chem.* **44** (1952) 2490–2496.
- [13] D. Zheng, B.-J. Zhong, P.-F. Xiong, Experimental study on laminar flame speeds and chemical kinetic model of 2,4,4-trimethyl-1-pentene, *Fuel* **229** (2018) 95–104.
- [14] J. Andrae, T. Kovács, Evaluation of adding an olefin to mixtures of primary reference fuels and toluene to model the oxidation of a fully blended gasoline, *Energy Fuels* **30** (2016) 7721–7730.
- [15] E. Hu, G. Yin, J. Ku, Z. Gao, Z. Huang, Experimental and kinetic study of 2,4,4-trimethyl-1-pentene and iso-octane in laminar flames, *Proc. Combust. Inst.* **37** (2019) 1709–1716.
- [16] Y. Li, C.-W. Zhou, K.P. Somers, K. Zhang, H.J. Curran, The oxidation of 2-butene: a high pressure ignition delay, kinetic modeling study and reactivity comparison with isobutene and 1-butene, *Proc. Combust. Inst.* **36** (2017) 403–411.
- [17] G. Yin, E. Hu, S. Huang, J. Ku, X. Li, Z. Xu, Z. Huang, Experimental and kinetic study of diisobutylene isomers in laminar flames, *Energy* **170** (2019) 537–545.
- [18] G. Yin, Z. Gao, E. Hu, Z. Xu, Z. Huang, Comprehensive experimental and kinetic study of 2, 4, 4-trimethyl-1-pentene oxidation, *Combust. Flame* **208** (2019) 246–261.
- [19] G. Yin, E. Hu, F. Yang, J. Ku, Z. Huang, Kinetics of H abstraction and addition reactions of 2,4,4-trimethyl-1-pentene by OH radical, *Fuel* **210** (2017) 646–658.
- [20] G. Yin, E. Hu, X. Li, J. Ku, Z. Gao, Z. Huang, Theoretical study of abstraction and addition reactions of 2,4,4-trimethyl-1-pentene with H and O(3P) Radical, *Energy Fuels* **32** (2018) 11831–11842.
- [21] A.R. Laich, G. Kim, E. Ninnemann, B. Almansour, S. Vasu, Shock tube and flame speed measurements of 2, 4, 4-trimethyl-1-pentene: a Co-optima biofuel, *J. Energy Resour. Technol.* **144** (2022) 112308.
- [22] A. Bodi, B. Sztáray, T. Baer, M. Johnson, T. Gerber, Data acquisition schemes for continuous two-particle time-of-flight coincidence experiments, *Rev. Sci. Instrum.* **78** (2007) 084102.
- [23] M. Johnson, A. Bodi, L. Schulz, T. Gerber, Vacuum ultraviolet beamline at the Swiss light Source for chemical dynamics studies, *Nucl. Instrum. Methods Phys. Res. Sect. A* **610** (2009) 597–603 Accelerators, Spectrometers, Detectors and Associated Equipment.
- [24] D.W. Kohn, H. Clauberg, P. Chen, Flash pyrolysis nozzle for generation of radicals in a supersonic jet expansion, *Rev. Sci. Instrum.* **63** (1992) 4003–4005.
- [25] Q. Guan, K.N. Urness, T.K. Ormond, D.E. David, G.B. Ellison, J.W. Daily, The properties of a micro-reactor for the study of the unimolecular decomposition of large molecules, *Int. Rev. Phys. Chem.* **33** (2014) 447–487.
- [26] S. Grimm, S.J. Baik, P. Hemberger, A. Bodi, A.M. Kempf, T. Kasper, B. Atakan, Gas-phase aluminium acetylacetonate decomposition: revision of the current mechanism by VUV synchrotron radiation, *Phys. Chem. Chem. Phys.* **23** (2021) 15059–15075.
- [27] A. Bodi, P. Hemberger, D.L. Osborn, B. Sztáray, Mass-resolved isomer-selective chemical analysis with imaging photoelectron photoion coincidence spectroscopy, *J. Phys. Chem. Lett.* **4** (2013) 2948–2952.
- [28] B. Sztáray, K. Voronova, K.G. Torma, K.J. Covert, A. Bodi, P. Hemberger, T. Gerber, D.L. Osborn, CRF-PEPICO: double velocity map imaging photoelectron photoion coincidence spectroscopy for reaction kinetics studies, *J. Chem. Phys.* **147** (2017) 013944.
- [29] P. Hemberger, A.J. Trevitt, E. Ross, G. da Silva, Direct observation of para-xylylene as the decomposition product of the meta-xylyl radical using VUV synchrotron radiation, *J. Phys. Chem. Lett.* **4** (2013) 2546–2550.
- [30] B. Sztáray, T. Baer, Suppression of hot electrons in threshold photoelectron photoion coincidence spectroscopy using velocity focusing optics, *Rev. Sci. Instrum.* **74** (2003) 3763–3768.
- [31] Y. Kim, B.D. Etz, G.M. Fioroni, C.K. Hays, P.C. St. John, R.A. Messerly, S. Vyas, B.P. Beekley, F. Guo, C.S. McEnally, L.D. Pfefferle, R.L. McCormick, S. Kim, Investigation of structural effects of aromatic compounds on sooting tendency with mechanistic insight into ethylphenol isomers, *Proc. Combust. Inst.* **38** (2021) 1143–1151.

- [32] B.D. Etz, G.M. Fioroni, R.A. Messerly, M.J. Rahimi, P.C. St. John, D.J. Robichaud, E.D. Christensen, B.P. Beekley, C.S. McEnally, L.D. Pfefferle, Y. Xuan, S. Vyas, R.S. Paton, R.L. McCormick, S. Kim, Elucidating the chemical pathways responsible for the sooting tendency of 1 and 2-phenylethanol, *Proc. Combust. Inst.* 38 (2021) 1327–1334.
- [33] M.S. Johnson, M.R. Nimlos, E. Ninnemann, A. Laich, G.M. Fioroni, D. Kang, L. Bu, D. Ranasinghe, S. Khanniche, S.S. Goldsborough, S.S. Vasu, W.H. Green, Oxidation and pyrolysis of methyl propyl ether, *Int. J. Chem. Kinet.* 53 (2021) 915–938.
- [34] J.F. Gardais, P. Gorin, A. Prevot, J. Serpinet, J. Tranchant, G. Uniz, Manuel Pratique De Chromatographie En Phase Gazeuse, 3e édition, Elsevier Masson, Paris, New York, Barcelona, 1982.
- [35] H. Nakamura, D. Darcy, M. Mehl, C.J. Tobin, W.K. Metcalfe, W.J. Pitz, C.K. Westbrook, H.J. Curran, An experimental and modeling study of shock tube and rapid compression machine ignition of n-butylbenzene/air mixtures, *Combust. Flame* 161 (2014) 49–64.
- [36] C. Morley, Gaseq, Available at <http://www.gaseq.co.uk/>, (2004).
- [37] V.A. Alekseev, J.D. Naucler, M. Christensen, E.J.K. Nilsson, E.N. Volkov, L.P.H. de Goey, A.A. Konnov, Experimental uncertainties of the heat flux method for measuring burning velocities, *Combust. Sci. Technol.* 188 (2016) 853–894.
- [38] ANSYS Chemkin-Pro 18.2, Ansys, San Diego, 2017.
- [39] M. Frisch, G. Trucks, H. Schlegel, G. Scuseria, M. Robb, J. Cheeseman, G. Scalmani, V. Barone, G. Petersson, H. Nakatsuji, <https://gaussian.com>, Gaussian 16, Gaussian, Inc., Wallingford CT, 2016.
- [40] L.A. Curtiss, P.C. Redfern, K. Raghavachari, Gaussian-4 theory, *J. Chem. Phys.* 126 (2007) 084108.
- [41] J.M. Simmie, K.P. Somers, Benchmarking compound methods (CBS-QB3, CB-S-APNO, G3, G4, W1BD) against the active thermochemical tables: a litmus test for cost-effective molecular formation enthalpies, *J. Phys. Chem. A* 119 (2015) 7235–7246.
- [42] K.P. Somers, J.M. Simmie, Benchmarking compound methods (CBS-QB3, CB-S-APNO, G3, G4, W1BD) against the active thermochemical tables: formation enthalpies of radicals, *J. Phys. Chem. A* 119 (2015) 8922–8933.
- [43] L.A. Curtiss, P.C. Redfern, K. Raghavachari, Assessment of Gaussian-4 theory for energy barriers, *Chem. Phys. Lett.* 499 (2010) 168–172.
- [44] G. Luchini, J.V. Alegre-Requena, I. Funes-Ardoiz, R.S. Paton, GoodVibes: automated thermochemistry for heterogeneous computational chemistry data, *F1000Res* 9 (2020) 291.
- [45] V.A. Mozhayskiy, A.I. Krylov, Ezspectrum, <http://iopshell.usc.edu/downloads>.
- [46] K. Wang, S.M. Villano, A.M. Dean, Experimental and kinetic modeling study of butene isomer pyrolysis: part II. Isobutene, *Combust. Flame* 176 (2017) 23–37.
- [47] W. Tsang, Thermal decomposition of cyclopentane and related compounds, *Int. J. Chem. Kinet.* 10 (1978) 599–617.
- [48] L. Ye, Y. Georgievskii, S.J. Klippenstein, Pressure-dependent branching in the reaction of  $1\text{CH}_2$  with  $\text{C}_2\text{H}_4$  and other reactions on the  $\text{C}_3\text{H}_6$  potential energy surface, *Proc. Combust. Inst.* 35 (2015) 223–230.
- [49] J.A. Miller, S.J. Klippenstein, Dissociation of propyl radicals and other reactions on a  $\text{C}_3\text{H}_7$  Potential, *J. Phys. Chem. A* 117 (2013) 2718–2727.
- [50] S.S. Vasu, L.K. Huynh, D.F. Davidson, R.K. Hanson, D.M. Golden, Reactions of OH with butene isomers: measurements of the overall rates and a theoretical study, *J. Phys. Chem. A* 115 (2011) 2549–2556.
- [51] J. Zádor, S.J. Klippenstein, J.A. Miller, Pressure-dependent OH yields in alkene +  $\text{HO}_2$  reactions: a theoretical study, *J. Phys. Chem. A* 115 (2011) 10218–10225.
- [52] C.-W. Zhou, J.M. Simmie, K.P. Somers, C.F. Goldsmith, H.J. Curran, Chemical kinetics of hydrogen atom abstraction from allylic sites by  $^3\text{O}_2$ ; implications for combustion modeling and simulation, *J. Phys. Chem. A* 121 (2017) 1890–1899.
- [53] J. Badra, A. Farooq, Site-specific reaction rate constant measurements for various secondary and tertiary H-abstraction by OH radicals, *Combust. Flame* 162 (2015) 2034–2044.
- [54] R. Sivaramakrishnan, J.V. Michael, Rate constants for OH with selected large alkanes: shock-tube measurements and an improved group scheme, *J. Phys. Chem. A* 113 (2009) 5047–5060.
- [55] S. Snitsiriwat, J.W. Bozzelli, Thermochemical properties for isooctane and carbon radicals: computational study, *J. Phys. Chem. A* 117 (2013) 421–429.
- [56] R.S. Tranter, A.W. Jasper, J.B. Randazzo, J.P.A. Lockhart, J.P. Porterfield, Recombination and dissociation of 2-methyl allyl radicals: experiment and theory, *Proc. Combust. Inst.* 36 (2017) 211–218.
- [57] P. Hemberger, A. Bodi, T. Bierkandt, M. Köhler, D. Kaczmarek, T. Kasper, Photoelectron photoion coincidence spectroscopy provides mechanistic insights in fuel synthesis and conversion, *Energy Fuels* 35 (2021) 16265–16302.
- [58] D. Felsmann, K. Moshhammer, J. Krüger, A. Lackner, A. Brockhinke, T. Kasper, T. Bierkandt, E. Akyildiz, N. Hansen, A. Lucassen, P. Oßwald, Electron ionization, photoionization and photoelectron/photoion coincidence spectroscopy in mass-spectrometric investigations of a low-pressure ethylene/oxygen flame, *Proc. Combust. Inst.* 35 (2015) 779–786.
- [59] P. Hemberger, M. Lang, B. Noller, I. Fischer, C. Alcaraz, B.K. Cunha de Miranda, G.A. Garcia, H. Soldi-Lose, Photoionization of propargyl and bromopropargyl radicals: a threshold photoelectron spectroscopic study, *J. Phys. Chem. A* 115 (2011) 2225–2230.
- [60] P. Hemberger, X. Wu, Z. Pan, A. Bodi, Continuous pyrolysis microreactors: hot sources with little cooling? New insights utilizing cation velocity map imaging and threshold photoelectron spectroscopy, *J. Phys. Chem. A* 126 (2022) 2196–2210.
- [61] T. Bierkandt, P. Hemberger, P. Oßwald, M. Köhler, T. Kasper, Insights in m-xylene decomposition under fuel-rich conditions by imaging photoelectron photoion coincidence spectroscopy, *Proc. Combust. Inst.* 36 (2017) 1223–1232.
- [62] M. Gerlach, A. Bodi, P. Hemberger, Metamorphic meta isomer: carbon dioxide and ketenes are formed via retro-Diels–Alder reactions in the decomposition of meta-benzenediol, *Phys. Chem. Chem. Phys.* 21 (2019) 19480–19487.
- [63] D. Krüger, P. Oßwald, M. Köhler, P. Hemberger, T. Bierkandt, T. Kasper, The fate of the OH radical in molecular beam sampling experiments, *Proc. Combust. Inst.* 37 (2019) 1563–1570.
- [64] D.D. Das, P.C.S. John, C.S. McEnally, S. Kim, L.D. Pfefferle, Measuring and predicting sooting tendencies of oxygenates, alkanes, alkenes, cycloalkanes, and aromatics on a unified scale, *Combust. Flame* 190 (2018) 349–364.
- [65] N. Lokachari, S. Panigrahy, G. Kukkadapu, G. Kim, S.S. Vasu, W.J. Pitz, H.J. Curran, The influence of iso-butene kinetics on the reactivity of di-isobutylene and iso-octane, *Combust. Flame* 222 (2020) 186–195.
- [66] X. Sun, W. Zong, J. Wang, Z. Li, X. Li, Pressure-dependent rate rules for cycloaddition, intramolecular H-shift, and concerted elimination reactions of alkenyl peroxy radicals at low temperature, *Phys. Chem. Chem. Phys.* 21 (2019) 10693–10705.
- [67] V.A. Alekseev, S.S. Matveev, I.V. Chechet, S.G. Matveev, A.A. Konnov, Laminar burning velocities of methylcyclohexane + air flames at room and elevated temperatures: a comparative study, *Combust. Flame* 196 (2018) 99–107.
- [68] V.A. Alekseev, M. Christensen, A.A. Konnov, The effect of temperature on the adiabatic burning velocities of diluted hydrogen flames: a kinetic study using an updated mechanism, *Combust. Flame* 162 (2015) 1884–1898.